The Astronomical Journal, 166:9 (21pp), 2023 July https://doi.org/10.3847/1538-3881/acd548

VaTEST. II. Statistical Validation of 11 TESS-detected Exoplanets Orbiting K-type Stars

Priyashkumar Mistry[1], Kamlesh Pathak[1], Aniket Prasad[2], Georgios Lekkas[3], Surendra Bhattarai[4], Sarvesh Gharat[5], Mousam Maity[6], Dhruv Kumar[2], Karen A. Collins[7], Richard P. Schwarz[7], Christopher R. Mann[8,9], Elise Furlan[10], Steve B. Howell[11], David Ciardi[10], Allyson Bieryla[7], Elisabeth C. Matthews[12], Erica Gonzales[13], Carl Ziegler[14], Ian Crossfield[15], Steven Giacalone[16], Thiam-Guan Tan[17,18], Phil Evans[19], Krzysztof G. Hełminiak[20], Kevin I. Collins[21], Norio Narita[22,23,24], Akihiko Fukui[22,24], Francisco J. Pozuelos[25], Courtney Dressing[16], Abderahmane Soubkiou[26], Zouhair Benkhaldoun[26], Joshua E. Schlieder[27], Olga Suarez[28], Khalid Barkaoui[29,30,31], Enric Palle[32,33], Felipe Murgas[32,33], Gregor Srdoc[34], Maria V. Goliguzova[35], Ivan A. Strakhov[35], Crystal Gnilka[11], Kathryn Lester[11], Colin Littlefield[11,36], Nic Scott[11], Rachel Matson[37], Michaël Gillon[29], Emmanuel Jehin[38], Mathilde Timmermans[29], Mourad Ghachoui[26,29], Lyu Abe[28], Philippe Bendjoya[28], Tristan Guillot[28], and Amaury H. M. J. Triaud[39]

[1] Department of Physics, Sardar Vallabhbhai National Institute of Technology, Surat-395007, Gujarat, India; priyashmistry10@gmail.com
[2] Department of Physics, National Institute of Technology Agartala 799046, Tripura, India
[3] Department of Physics, University of Ioannina, Ioannina, 45110, Greece
[4] Department of Physics, Indian Institute of Science Education and Research Kolkata, Mohanpur-741246, West Bengal, India
[5] Centre for Machine Intelligence and Data Science, Indian Institute of Technology Bombay, India
[6] Department of Physics, Presidency University, Kolkata-700073, West Bengal, India
[7] Center for Astrophysics | Harvard & Smithsonian, 60 Garden Street, Cambridge, MA 02138, USA
[8] Département de physique, Université de Montréal, 1375 Avenue Thérèse-Lavoie-Roux, Montréal, Québec, H3T 1J4, Canada
[9] Trottier Institute for Research on Exoplanets (*iREx*), Canada
[10] NASA Exoplanet Science Institute, Caltech/IPAC, Mail Code 100-22, 1200 E. California Boulevard, Pasadena, CA 91125, USA
[11] NASA Ames Research Center, Moffett Field, CA 94035, USA
[12] Max-Planck-Institut für Astronomie, Königstuhl 17, D-69117 Heidelberg, Germany
[13] Department of Astronomy and Astrophysics, University of California Santa Cruz, Santa Cruz, CA 95064, USA
[14] Department of Physics, Engineering and Astronomy, Stephen F. Austin State University, 1936 North Street, Nacogdoches, TX 75962, USA
[15] Department of Physics & Astronomy, University of Kansas, KS 66045, USA
[16] Department of Astronomy, University of California Berkeley, Berkeley, CA 94720, USA
[17] Perth Exoplanet Survey Telescope, Perth, Western Australia, Australia
[18] Curtin Institute of Radio Astronomy, Curtin University, Bentley, Western Australia 6102, Australia
[19] El Sauce Observatory, Coquimbo Province, Chile
[20] Nicolaus Copernicus Astronomical Center, Polish Academy of Sciences, ul. Rabiańska 8, 87-100 Toruń, Poland
[21] George Mason University, 4400 University Drive, Fairfax, VA, 22030 USA
[22] Komaba Institute for Science, The University of Tokyo, 3-8-1 Komaba, Meguro, Tokyo 153-8902, Japan
[23] Astrobiology Center, 2-21-1 Osawa, Mitaka, Tokyo 181-8588, Japan
[24] Instituto de Astrofisica de Canarias (IAC), E-38205 La Laguna, Tenerife, Spain
[25] Instituto de Astrofísica de Andalucía (IAA-CSIC), Glorieta de la Astronomía s/n, E-18008 Granada, Spain
[26] Oukaimeden Observatory, High Energy Physics and Astrophysics Laboratory, Cadi Ayyad University, Marrakech, Morocco
[27] NASA Goddard Space Flight Center, 8800 Greenbelt Road, Greenbelt, MD 20771, USA
[28] Université Côte d'Azur, Observatoire de la Côte d'Azur, CNRS, Laboratoire Lagrange, Bd de l'Observatoire, CS 34229, F-06304 Nice cedex 4, France
[29] Astrobiology Research Unit, Université de Liège, 19C Allée du 6 Aot, B-4000 Liège, Belgium
[30] Department of Earth, Atmospheric and Planetary Science, Massachusetts Institute of Technology, 77 Massachusetts Avenue, Cambridge, MA 02139, USA
[31] Instituto de Astrofísica de Canarias (IAC), Calle Vía Láctea s/n, E-38200, La Laguna, Tenerife, Spain
[32] Instituto de Astrofísica de Canarias (IAC), E-38205 La Laguna, Tenerife, Spain
[33] Departamento de Astrofísica, Universidad de La Laguna (ULL), E-38206, La Laguna, Tenerife, Spain
[34] Kotizarovci Observatory, Sarsoni 90, 51216 Viskovo, Croatia
[35] Sternberg Astronomical Institute, M.V. Lomonosov Moscow State University, 13, Universitetskii pr., 119234, Moscow, Russia
[36] Bay Area Environmental Research Institute, Moffett Field, CA 94035, USA
[37] U.S. Naval Observatory, Washington, D.C. 20392, USA
[38] Space Sciences, Technologies and Astrophysics Research (STAR) Institute, Université de Liège, 19C Allée du 6 Aot, B-4000 Liège, Belgium
[39] School of Physics & Astronomy, University of Birmingham, Edgbaston, Birmingham B15 2TT, UK; priyashmistry10@gmail.com
Received 2023 January 30; revised 2023 May 10; accepted 2023 May 12; published 2023 June 12

Abstract

NASA's Transiting Exoplanet Survey Satellite (TESS) is an all-sky survey mission designed to find transiting exoplanets orbiting nearby bright stars. It has identified more than 329 transiting exoplanets, and almost 6000 candidates remain unvalidated. In this manuscript, we discuss the findings from the ongoing Validation of Transiting Exoplanets using Statistical Tools (VaTEST) project, which aims to validate new exoplanets for further characterization. We validated 11 new exoplanets by examining the light curves of 24 candidates using the `LATTE` and `TESS-Plot` tools and computing the false-positive probabilities using the statistical validation tool `TRICERATOPS`. These include planets suitable for atmospheric characterization using transmission spectroscopy

(TOI-2194b), emission spectroscopy (TOI-3082b and TOI-5704b) and for both transmission and emission spectroscopy (TOI-672b, TOI-1694b, and TOI-2443b). Our validated planets have one super-Earth (TOI-2194b) orbiting a bright ($V = 8.42$ mag), metal-poor ([Fe/H] $= -0.3720 \pm 0.1$) star, and one short-period Neptune-like planet (TOI-5704) in the hot-Neptune desert. In total, we validated one super-Earth, seven sub-Neptunes, one Neptune-like, and two sub-Saturn or super-Neptune-like exoplanets. Additionally, we identify five likely planet candidates (TOI-323, TOI-1180, TOI-2200, TOI-2408, and TOI-3913), which can be further studied to establish their planetary nature.

Unified Astronomy Thesaurus concepts: Exoplanet astronomy (486); Exoplanet systems (484); Exoplanet detection methods (489)

1. Introduction

The Transiting Exoplanet Survey Satellite (TESS; Ricker et al. 2015) mission is an all-sky survey to discover exoplanets in nearby regions. It was launched on 2018 April 18 aboard a SpaceX Falcon 9 rocket. During its two-year primary mission, the TESS spacecraft concentrated on nearby G-, K-, and M-type stars with apparent magnitudes <12. An area 400 times greater than the one covered by the Kepler campaign was to be surveyed, including the 1000 nearest dwarf stars in the entire sky. The survey was divided into 26 viewing zones called sectors, each of which was $24° \times 96°$. The spacecraft had spent two 13.7 days orbiting each sector, mapping the southern hemisphere in its first year of operation and the northern hemisphere in its second year. TESS's primary mission (cycles 1 and 2, sectors 1–26) was completed in 2020 July. The first extended mission (cycles 3 and 4, sectors 27–55) ended in 2022 September, and it is now on its second extended mission (cycle 5, sectors 56–69).

We currently have 323 confirmed TESS exoplanets and 6386 TESS candidates[40] that need to be studied. By using the conventional method, i.e., a combination of transit and radial velocity to discover a new planet, it is very difficult to study this large number of candidates. There are so-called astrophysical false positives (Brown 2003; Cameron 2012), such as eclipsing binaries, blended eclipsing binaries, and planet-sized stars in binary systems that can generate a transit-like signal. Many tools have been developed based on transit photometry to calculate their likelihood and probability of being planets or false positives. To rule out false positives, `BLENDER` (Torres et al. 2005) was the first approach based on χ^2 statistics of eclipsing binaries and blended eclipsing binaries. Bryson et al. (2013) has presented various tests to rule out the possibility of blended eclipsing binaries. These methods include photometric centroid shift, difference imaging, and pixel correlation images. In the first method the centroid shift is detected on the pixels correlated with transit signal and that shift is then used to estimate the location of the transit source. The second method uses the difference image of in- and out-of-transit pixel image to locate the transit source and the last method computes the degree to which the transit signal over time appears in each pixel. These methods make an assumption that the transit signal is solely created by the pixels under investigation (i.e., the mean flux from the TESS aperture mask pixels) and that there are no other sources of flux variation. However, when this assumption is violated, these techniques may introduce systematic errors. The nature of these errors may differ among the methods utilized. Thus, the presence of inconsistencies in the outcomes obtained from these techniques may indicate the existence of systematic error. `VESPA` (Morton 2015) was another approach that used the MCMC sampling routine to fit the Kepler light curve and produced a false-positive probability based on the fit. Both `VESPA` and `BLENDER` can include high-contrast imaging in their analysis. The framework was widely used to statistically validate exoplanets from Kepler as well as TESS. The another robust model `PASTIS` (Díaz et al. 2014), which can take transit photometry data as well as high-precision radial velocity measurements to validate the planet. Alternatively, `TRICERATOPS` (Giacalone & Aressing 2020; Giacalone et al. 2021) was specifically developed to take advantage of the unique features and requirements of the TESS mission. With a lower resolution than previous such missions, there may be a greater necessity to account for multiple star systems and scenarios like diluted transits. Such approaches can be used to validate new exoplanets in bulk without having radial velocity measurements. For our project, we made use of `TRICERATOPS` as a validation tool to calculate the false-positive probability (FPP) of selected candidates.

The Validation of Transiting Exoplanets using Statistical Tools project[41] has its primary goal to validate multiple exoplanets with the use of various statistical validation approaches. In our first paper, we discovered our first planet, TOI-181b (Mistry et al. 2023), by utilizing a similar approach. For the future, we have separated candidates based on their spectral types (temperatures) and will study them each individually in order to find out their planetary nature. However, for this manuscript, we will validate the exoplanets orbiting K-type (temperature range 3700–5200 K; Habets & Heintze 1981; Weidner & Vink 2010) stars. Here we validated a significant number of exoplanets from the candidates observed by TESS.

This paper is structured as follows: In Section 2 we discuss our methodology to select the most promising candidates for the validation process, and in Section 3 we present the high-resolution imaging and ground-based photometic observations. The algorithm and procedure for using the statistical validation tool `TRICERATOPS` is covered in Section 4. In Section 5 we presented the main features of newly validated systems. Finally, Section 6 describes candidates that failed the validation criteria (not validated candidates) and some likely planets that can be followed up further to validate.

2. Selection of Candidates

In this manuscript, we study planets orbiting K-spectral-type stars. There were multiple restrictions made while selecting the targets for our study, such as:

1. Reported orbital period <20 days.
2. Planetary radii $<8R_E$.

[40] https://exoplanetarchive.ipac.caltech.edu/, accessed on 2023 April 19.

[41] https://sites.google.com/view/project-vatest/home

3. Removed targets with the dispositions (from ExoFOP[42]) confirmed planet, known planet, false positive, and eclipsing binary.

As we based our validations on a combination of high-resolution imaging, ground-based photometry, and transit photometry data, it is crucial to ensure that the light curve contains a maximum number of transits to confirm the exoplanetary nature of a signal. The minimum number of transits required to confirm the existence of an exoplanet is typically at least three, so we make sure that all of the considered targets had at least 3 transits, either in a single sector or in a combination of different sectors. For this reason we choose targets showing <20 days orbital period. The major reason behind having radii $<8R_E$ is the statistical validation tool called TRICERATOPS (Giacalone et al. 2021). TRICERATOPS underpredicts the FPP for planetary candidates having radii $\geqslant 8R_E$.

A total of 343 candidates from the Exoplanet Follow-up Observing Program (ExoFOP) website database are considered in this study. To identify possible binary stars, use of Renormalized Unit Weight Error (RUWE) score (Lindegren 2018) from Gaia EDR3 is done. Targets with an RUWE score of $\geqslant$1.4 or null (Lindegren 2018) are eliminated. Additionally, targets with stellar companions, lacking SPOC pipeline data, or without available stellar parameters were also excluded from this study. A visual inspection of the remaining targets was performed to eliminate any signals that were consistent with star variability, eclipsing binaries, or instrumental systematic effects. Finally, the use of Juliet modeling (Espinoza et al. 2018) is done on the remaining set of targets to identify eclipsing binaries based on the shape (V-shaped) and characteristics of modeled transit light curves. Through this initial screening process, a total of 24 significant objects were identified for further examination of their planetary nature. Stellar parameters for these selected targets are shown in Table 1. We have taken stellar parameters from ExoFOP website, which were derived using one of the three methods. First is stellar spectra collected using Fred Lawrence Whipple Observatory (FLWO). FLWO spectra were obtained at the Fred Lawrence Whipple Observatory using the Tillinghast Reflector Echelle Spectrograph (TRES; Fűrész 2008) on the 1.5 m Tillinghast Reflector telescope. Stellar parameters were derived using the stellar parameter classification tool as outlined in Buchhave et al. (2012, 2014). Second is Nordic Optical Telescope's high-resolution FIbre-fed Echelle Spectrograph (Telting et al. 2014). FIES is a cross-dispersed high-resolution echelle spectrograph with a maximum spectral resolution of $R = 67{,}000$. The entire spectral range 370–830 nm is covered without gaps in a single, fixed setting. And the third is ExoFASTV2 tool (Eastman et al. 2019). For some of the targets parameters were not available from either of the method, in such cases we used the values from TESS Input Catalog (TIC; Stassun et al. 2018) stellar parameters (version 8.2; Stassun et al. 2019). In particular all the radii and masses are taken the from TIC stellar parameters.

Before conducting a thorough and computationally expensive probabilistic analysis for transit signals, it is important to check the origin of the detected signal preliminarily. We employed the open source package Lightcurve Analysis Tool for Transiting Exoplanet (LATTE; Eisner 2022), which runs multiple diagnostic tests providing an approximate indication that the signal may be originating from the target star rather than any nearby sources. We discuss our interpretation of these tests in Section 2.1. However, it should be noted that this preliminary test provides only approximate information and does not provide a high level of confidence regarding the origin of the signal. Further analysis and verification are required. The results of the LATTE tests for all of the considered candidates have been uploaded to a publicly available GitHub repository[43] for further examination. After reviewing the results of LATTE analysis we have concluded that transit signal and star are approximately corelated. To confirm the planetary nature of the given signal we have used statistical validation tool TRICERATOPS. Methodology and results are discussed in Sections 4.1 and 5.

2.1. Results of Diagnostic Tests

The LATTE program performs multiple tests on a chosen TESS target by considering all the transit events observed by the TESS to be passed through diagnosis. Taking inspiration from SPOC pipeline data validation, LATTE performs multiple checks for background flux, in-out transit flux, pixel-level light curves, and centroid correlation/positions for each transit. The checks at the level of each transit event being tested individually help us to rule out any possible false alarms, or account for any instrumental error affecting transits.

We utilized comparative plots of background flux and overall flux to rule out the possibility of any background object such as a solar system object or asteroid in line of sight mimicking a transit-like event. Each time TESS attains the perigee of its eccentric orbit around the Earth enhanced scattered light in the telescope optics can cause the background flux to sharply increase. We therefore look at the background plots to ensure that there are no spikes at the time of the transit-like events. Figure 1 simultaneously shows the transit event and the background flux for TOI-672 (Sector-09). There is no obvious change in the background flux that is correlated with the transit signals. Also, no correlations were seen in any other TESS object of interest (TOI) light curves.

Another diagnostic test we have used as a filter in this work is generating in- and out-of-transit flux comparison plots. We have used TESS-Plot[44] package to generate the plots. By analyzing the difference images, we were able to determine whether the observed transit-like signal was related to the target star or if it was occurring due to a background source such as an eclipsing binary or a nearby transiting planet. If the change in brightness occurred on the target star pixel, then it was indicative that the signal may be related to the target star. However, if the change in brightness occurred elsewhere on the image, it was evident that the transit-like signal was occurring due to an off-target source. Figure 2 displays the difference image for our target, TOI-672. As can be observed from the figure, the change in brightness is on our selected target (indicated by the star symbol, other dots represent the nearby stars). For all the TOIs there exists an approximate correlation between the transit signal and the target star.

We also considered the location of the row and column centroid at each transit event as shown in Figure 3 centroid plot for TOI-672. The centroid is the point in aperture where the

[42] https://exofop.ipac.caltech.edu/tess

[43] https://github.com/priyashmistry/VaTEST-II-Output-Files.git

[44] https://github.com/mkunimoto/TESS-plots

Table 1
Stellar Parameters of the Candidate Systems

No.	TOI ID	TIC ID	$T_{\rm eff}$ (K)	R_s ($R_\odot$)	M_s ($M_\odot$)	log$g$	[Fe/H][a] (dex)	V (mag)	TESS (mag)	RUWE	Source[b]
1	TOI 139	62483237	4570 ± 50	0.7007 ± 0.0575	0.6900 ± 0.0852	4.705 ± 0.100	-0.238 ± 0.080	10.55	9.36	0.8818	TRES, TIC
2	TOI 323	251852984	4558 ± 122	0.7756 ± 0.1000	0.7370 ± 0.0455	4.613 ± 0.027	-0.040 ± 0.325	14.35	13.35	1.0132	ExoFASTv2, TIC
3	TOI 493	19025965	4402 ± 100	0.8119 ± 0.0661	0.6480 ± 0.0829	4.689 ± 0.100	-0.181 ± 0.080	12.55	11.45	1.1079	TRES, TIC
4	TOI 672	151825527	3765 ± 65	0.5441 ± 0.0163	0.5399 ± 0.0204	4.699 ± 0.010	-0.710 ± 0.625	13.58	11.67	1.1587	TIC
5	TOI 815	102840239	4954 ± 107	0.7594 ± 0.0426	0.8200 ± 0.0943	4.591 ± 0.081	0.037 ± 0.039	10.22	9.36	1.0129	TIC
6	TOI 913	407126408	4969 ± 129	0.7325 ± 0.0488	0.8200 ± 0.0973	4.622 ± 0.089	-0.133 ± 0.100	10.45	9.62	1.0136	TIC
7	TOI 1179	148914726	4998 ± 50	0.7770 ± 0.0110	0.8050 ± 0.4450	4.462 ± 0.100	-0.084 ± 0.080	10.88	10.13	1.0336	FIES, ExoFASTv2
8	TOI 1180	158002130	4900 ± 50	0.7272 ± 0.0518	0.7500 ± 0.0934	4.723 ± 0.100	-0.024 ± 0.080	11.02	10.11	0.9415	TRES, TIC
9	TOI 1694	396740648	5135 ± 50	0.8183 ± 0.0477	0.8450 ± 0.1089	4.658 ± 0.100	0.060 ± 0.080	11.45	10.74	1.3827	TRES, TIC
10	TOI 1732	470987100	3876 ± 157	0.6326 ± 0.0187	0.6139 ± 0.0203	4.624 ± 0.011	0.291 ± 0.100	12.89	11.33	1.3104	TIC
11	TOI 2194	271478281	4756 ± 50	0.6909 ± 0.0492	0.7400 ± 0.0854	4.698 ± 0.100	-0.372 ± 0.100	8.42	7.43	0.9936	TRES, TIC
12	TOI 2200	142105158	5070 ± 117	0.8262 ± 0.0487	0.8500 ± 0.1038	4.533 ± 0.084	0.273 ± 0.100	13.09	12.32	1.0810	TIC
13	TOI 2408	67630845	4935 ± 132	0.7485 ± 0.0510	0.8100 ± 0.0969	4.598 ± 0.092	⋯	12.78	11.92	1.0093	TIC
14	TOI 2443	318753380	4357 ± 100	0.7321 ± 0.0713	0.6600 ± 0.0789	4.709 ± 0.100	-0.439 ± 0.080	9.51	8.30	1.2536	TRES, TIC
15	TOI 2459	192790476	4195 ± 124	0.6751 ± 0.0630	0.6600 ± 0.0763	4.599 ± 0.107	⋯	10.77	9.40	1.1358	TIC
16	TOI 3082	428699140	4263 ± 100	0.6847 ± 0.0613	0.6640 ± 0.0798	4.625 ± 0.100	0.170 ± 0.080	12.93	11.77	1.2058	TRES, TIC
17	TOI 3568	160390955	4890 ± 50	0.7858 ± 0.0517	0.7920 ± 0.0942	4.540 ± 0.100	0.002 ± 0.080	12.88	12.07	0.9779	TRES, TIC
18	TOI 3896	445837596	5043 ± 50	0.7478 ± 0.0431	0.8600 ± 0.1032	4.419 ± 0.100	-0.279 ± 0.080	12.43	11.68	0.9606	TRES, TIC
19	TOI 3913	155898758	4180 ± 123	0.8257 ± 0.0767	0.6540 ± 0.0813	4.420 ± 0.110	0.137 ± 0.110	13.71	12.58	1.0625	TIC
20	TOI 4090	289373041	4740 ± 124	0.8194 ± 0.0567	0.7600 ± 0.0909	4.492 ± 0.095	0.760 ± 0.091	13.40	12.55	1.0152	TIC
21	TOI 4308	144193715	5243 ± 126	0.7934 ± 0.0465	0.9000 ± 0.1133	4.593 ± 0.087	⋯	11.25	10.34	0.8720	TIC
22	TOI 5584	29169215	4372 ± 100	0.7451 ± 0.0684	0.6400 ± 0.0789	4.725 ± 0.100	0.128 ± 0.065	15.83	10.73	1.0809	TRES, TIC
23	TOI 5704	148673433	4590 ± 126	0.7575 ± 0.0593	0.7300 ± 0.0846	4.543 ± 0.095	0.428 ± 0.100	11.53	10.61	1.2287	TIC
24	TOI 5803	466382581	5134 ± 121	0.7625 ± 0.0451	0.8700 ± 0.1032	4.613 ± 0.085	⋯	10.66	9.94	0.9834	TIC

Notes.
[a] TRES derives [m/H], not [Fe/H]. In other words it derives a mixture of metals and not just Fe, which is an important distinction to note when comparing the metallicity of different objects.
[b] In the source column, wherever TIC is included, the radius and mass are taken from TICv8.2, while the rest of the parameters are taken from the other sources listed.

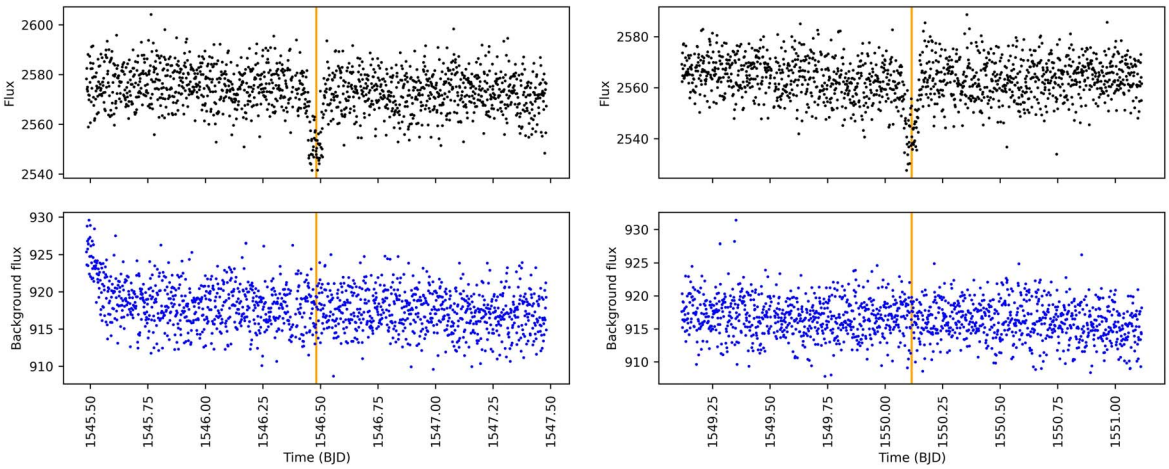

Figure 1. TOI-672 Sector-09 background flux at the time of first two transits. No spikes are observed at the time of transit.

average amount of light from the stars fall. Since a false-positive scenario like blended binary could result visible change in the position of centroid, We created diagnostic plots to track the target's row and column positions throughout each transit. However, no significant differences were found upon visual inspection. It is to note that the targets with almost similar magnitude within the aperture might still show correlations in centroid positions and hence, despite the apparent lack of visual shifts, it is imperative to account for nearby neighbors while performing validation.

Hence, the insights from these diagnostic tests helped increase our confidence to follow up with `TRICERATOPS` for a deeper analysis. The results of these tests for other candidates have been uploaded in GitHub. By observing those plots, it is inferred that the source of the transit-like signal is approximately related to the target pixel. Furthermore, we performed ground-based follow-up observations, high-resolution imaging, and false-positive probability calculation using `TRICERATOPS` to validate the planetary nature of the given transit signal.

3. Follow-up Observations

3.1. High-resolution Imaging

By utilizing adaptive optics and speckle imaging techniques, we captured high-contrast images of our TOIs. The observations were conducted by the members of TFOP Sub Group 3 (SG3) and are presented in Table 2, illustrated in Figure 4, and elaborated below.

3.1.1. Gemini-N/'Alopeke, Gemini-N/NIRI, and Gemini-S/Zorro

Speckle interferometric observations for TOI-139, TOI-323, TOI-493, TOI-672, TOI-815, TOI-913, TOI-1179, TOI-1694, TOI-1732, and TOI-2443 were performed by 'Alopeke and Zorro, installed at the calibration ports at Gemini North and South (e.g., see Horch et al. 2009; Scott et al. 2021). The full set of observations taken in 562 nm ($\Delta\lambda = 54$ nm) and 832 nm ($\Delta\lambda = 40$ nm) was then combined in Fourier space to produce their power spectrum and autocorrelation functions. The data reduction pipeline produces final data products that include 5σ contrast curves and reconstructed images (Howell et al. 2011). Contrast curves are presented in Figure 4. No secondary sources were detected within the reconstructed images.

3.1.2. Keck/NIRC2

High-resolution imaging observations for TOI-139, TOI-493, and TOI-1694 were made on UT 2018 September 18, 2019 March 25, and 2020 September 9, respectively, using NIRC2 (Sakai et al. 2020), which is situated on Keck II's left Nasmyth Platform (Wizinowich et al. 2000), behind the AO bench. By injecting simulated sources in 45° azimuthal incremenrs at discrete separations that were integer multiples of the full width at half maximum (FWHM) of the central source, we measured the sensitivity of the companions (Furlan et al. 2017; Schlieder et al. 2021). To determine the contrast sensitivity, the flux of each simulated source was raised until aperture photometry provided a detection of 5σ. Averaging all of the limits at that separation resulted in the final contrast sensitivity as a function of separation. Observations for TOI-139 were made in the BrGamma (λ_0= 2.168; $\Delta\lambda$ = 0.033 μm) and Jcont (λ_0= 1.213; $\Delta\lambda$ = 0.019 μm) filters, TOI-1694 was observed using Ks (λ_0 = 2.146; $\Delta\lambda = 0.311$ μm) filter, and TOI-493 was observed using BrGamma filter. The Keck AO observations revealed no additional stellar companions to within a resolution of $\approx 0\farcs5$ FWHM.

3.1.3. Palomar/PHARO

PHARO (Hayward et al. 2001) is a near-infrared camera made to work with the 200-inch Hale telescope at Palomar Observatory and the Palomar Adaptive Optics system. Detector has 1024 × 1024 Rockwell HAWAII HgCdTe pixel array with wavelength sensitivity of 1–1.25 microns. It has diffraction-limited angular resolutions of $0\farcs063$ and $0\farcs11$ for J- and K-band imaging, respectively. Its large-format detector has a field of view of $25''$–$40''$. AO images for TOI-1732, TOI-2443, TOI-3568, TOI-3896, TOI-3913, and TOI-4090 were collected in BrGamma (λ_0= 2.166; $\Delta\lambda$ = 0.02 μm) using the PHARO instrument. Estimated contrasts at different separations are presented in Table 2, No secondary sources were detected within the reconstructed images.

3.1.4. Shane/ShARCS

We observed TIC 470987100 (TOI-1732) on UT 2020 December 01 using the ShARCS camera on the Shane 3 meter telescope at the Lick Observatory (Kupke et al. 2012; Gavel et al. 2014; McGurk et al. 2014). Observations were taken with

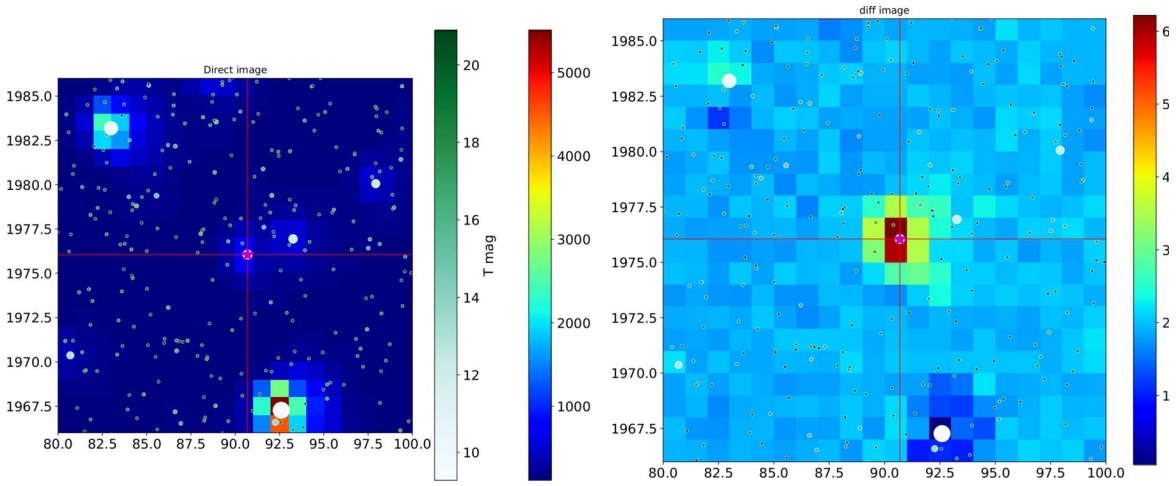

Figure 2. Difference between in and out transit flux for TOI-672. Left: Direct Image, Right: Difference Image. It can be understood by observing these images that variation in the brightness and target are approximately corelated.

the Shane adaptive optics system in natural guide star mode in order to search for nearby, unresolved stellar companions. We collected sequences of observations using K_S filter ($\lambda_0 = 2.150\ \mu$m, $\Delta\lambda = 0.320\,\mu$m). We reduced the data using the publicly available `SImMER` pipeline (Savel et al. 2020, 2022).[45] Our reduced images and corresponding contrast curves are shown in Figure 4. Our observations achieve contrasts of 4.5 (Brγ) and 2.7 (J) at 1″. We find no nearby stellar companions within our detection limits.

3.1.5. SOAR/HRCam

A high-resolution camera (HRCam) that can observe the 9.″9 × 7.″5 field of the sky has a 658 × 496 pixel array, with each pixel able to collect light from a 15 mas region (Tokovinin et al. 2010). This instrument was used to collect the speckle imaging observations for TOI-2194, TOI-2459, TOI-4308 and TOI-5803. It is a fast imager designed to work at the SOAR telescope, which uses a CCD detector with internal electron-multiplication. These observations and their related analyses are outlined in (Ziegler et al. 2020, 2021). We suggest the reader to those papers for more information.

3.1.6. VLT/NaCo

Observations for TOI-323 was performed using NaCo instrument with K filter. NaCo is the Paranal Observatory's instrument, which is a combination of Nasmyth Adaptive Optics System (Rousset et al. 2000) and CONICA (Lenzen et al. 1998) installed on the Very Large Telescope (VLT). It is able to compensate for the atmospheric variabilities and provides a diffraction-limited resolution for observing wavelengths ranging from 1 to 5 microns. It can collect imaging data with broad and narrow band filters, a field of view of 14″–56″, and a pixel scale of 13–54 mas per pixel.

3.1.7. SAI/Speckle Polarimeter

We observed TOI-1180 on 2020 December 02 UT with the Speckle Polarimeter (Safonov et al. 2017) on the 2.5 m telescope at the Caucasian Observatory of Sternberg Astronomical Institute (SAI) of Lomonosov Moscow State University. SPP uses Electron Multiplying CCD Andor iXon 897 as a detector. The atmospheric dispersion compensator allowed observation of this relatively faint target through the wide-band I_c filter. The power spectrum was estimated from 4000 frames with 30 ms exposure. The detector has a pixel scale of 20.6 mas pixel^{-1}, and the angular resolution was 89 mas. We did not detect any stellar companions brighter than $\Delta I_C = 4$ and 7.2 at $\rho = 0.''25$ and 1.″0, respectively, where ρ is the separation between the source and the potential companion.

3.2. Light-curve Follow-up Observations

The TESS pixel scale is ∼21″ pixel^{-1} and photometric apertures typically extend out to roughly 1′, generally causing multiple stars to blend in the TESS aperture. To rule out a nearby eclipsing binary (NEB) or shallower nearby planet candidate blend as the potential source of a TESS detection and attempt to detect the signal on target, we observed our target stars and the nearby fields as part of the TESS Follow-up Observing Program[46] Sub Group 1 (TFOP; Collins 2019). In some cases, we also observed in multiple bands across the optical spectrum to check for wavelength dependent transit depth differences, which can be suggestive of a planet candidate false positive. We used the `TESS Transit Finder`, which is a customized version of the `Tapir` software package (Jensen 2013), to schedule our transit observations.

All of our light-curve follow-up observations are summarized in Table 3 and all light-curve data are available on the `EXOFOP-TESS` website.[47] We also provide a short summary of each light-curve result and an overall final photometric follow-up disposition in Table 3. We assign four light-curve follow-up dispositions (PC, CPC, VPC, VPC+) to indicate differing levels of confidence that a TESS detection is on target, as described below.

The planet candidate (PC) disposition indicates that we either have no light-curve follow-up observations, or the light-curve observations are unable to confirm that the TESS-

[45] https://github.com/arjunsavel/SImMER

[46] https://tess.mit.edu/followup

[47] https://exofop.ipac.caltech.edu/tess

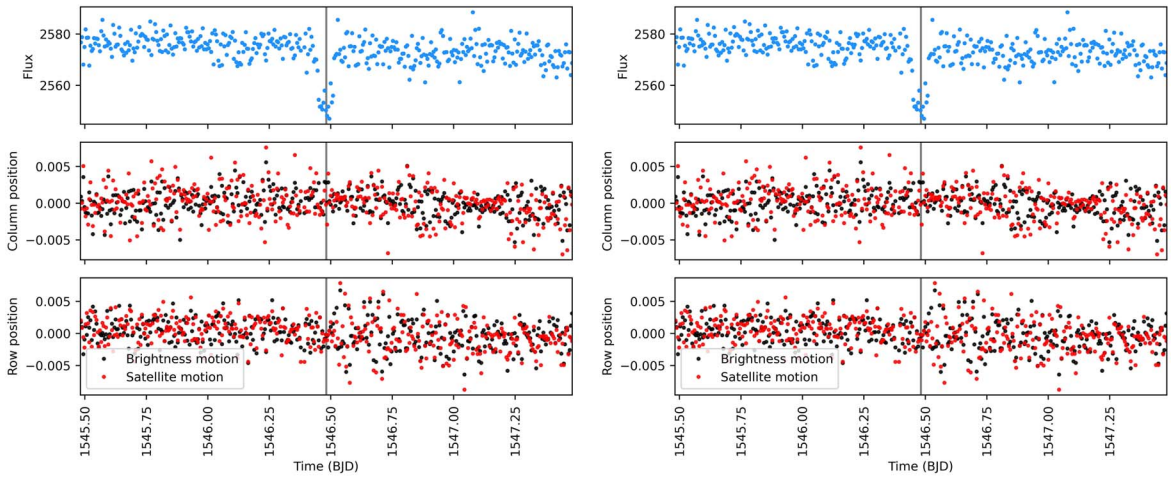

Figure 3. Centroid raw and column position at transit events.

detected event is on target relative to Gaia DR3 and TIC version 8 stars.

The cleared planet candidate (CPC) disposition indicates that we have confined the TESS detection to occur on the target star relative to all Gaia DR3 and TIC version 8 stars. Using ground-based photometry, we check all stars out to 2.′5 from the target star that are bright enough, assuming a 100% eclipse, in TESS-band to produce the TESS-detected depth at midtransit. To account for possible delta-magnitude differences between TESS-band and the follow-up band, and to account for TESS-band magnitude errors, we included an extra 0.5 magnitudes fainter in the TESS band. For these cases, the transit depth is generally too shallow to detect on target in ground-based follow-up observations, so we often saturate the target star on the detector to enable a complete search of all necessary fainter nearby stars. Since the TESS point-spread-function has full width half maximum of $\sim 40''$, and the irregularly shaped SPOC photometric apertures and circular QLP photometric apertures generally extend to $\sim 1'$ from the target star, we check for events in stars out to 2.′5 from the target star. For a star to be considered "cleared" of an NEB signal, we require its light curve to have an flat model residual rms value to be at least a factor of 3 smaller than the eclipse depth required to produce the TESS detection in the star. We ensure that the predicted ephemeris uncertainty is covered by at least $\pm 3\sigma$ relative to the most precise SPOC or QLP ephemeris available at the time of publication. Finally, we check all nearby starlight curves by eye to ensure that no obvious eclipse-like event is present. By process of elimination, we conclude that when all necessary nearby stars are "cleared" of NEBs, the transit is indeed occurring on target, or in a star so close to the target star, that it was not detected by Gaia DR3 and is not in TIC version 8.

The verified planet candidate (VPC) disposition indicates that we have confirmed using ground-based follow-up light-curve photometry that the TESS-detected event is occurring on target. This is accomplished using follow-up photometric apertures that are small enough to exclude most or all of the flux from the nearest Gaia DR3 and/or TIC version 8 star that is bright enough to be capable of producing the TESS signal.

The verified planet candidate plus (VPC+) disposition is the same as VPC, except we have measured transit depths in the target star follow-up photometric apertures across several optical bands. We elevate the disposition to VPC+ if no strong ($>3\sigma$) transit depth difference is detected across the bands.

4. Statistical Validation

With the advent of dedicated space missions for finding exoplanets, the number of possible planet-like candidates has increased rapidly. This creates a potential bottleneck between finding an exoplanet candidate and confirming the discovery with multiple follow-up observations. It is expected that TESS alone would be adding 12,000 potential exoplanets in the database over its 7 yr extended mission lifetime (Kunimoto et al. 2022). As a result, statistical validation of exoplanets becomes a viable alternative to confirming each candidate with dedicated observations with follow-up telescopes. Furthermore, statistical validation of such likely candidates could also act as a vetting and prioritization procedure for space missions and surveys such as `JWST` (Gardner et al. 2006), `CHEOPS` (Fortier 2014), or upcoming `PLATO` (Rauer et al. 2022). The constant improvement in knowledge of exoplanets occurrence rates and studies related to stellar populations have been utilized to derive a statistical threshold for confidently validating transit events as exoplanets. Various codes have been developed over the years with this objective such as `Pastis` (Díaz et al. 2014), `DAVE` (Kostov et al. 2019), `VESPA` (Morton 2015), and `TRICERATOPS` (Giacalone & Aressing 2020).

`VESPA` can be used if there are no known stars within the maximum radius (`maxrad`). For our selected targets there are known nearby targets within the `maxrad`, due to this reason it is not possible to use `VESPA` for the validation process. We have chosen `TRICERATOPS`, which was developed recently with a focus on the specifics of the TESS mission profile adding to features of `VESPA`. It has shown positive results for validations of TESS candidates (Giacalone et al. 2021). Unlike `VESPA`, `TRICERATOPS` includes known nearby stars in its analysis. Further details about this tool is provided in Section 4.1.

4.1. Validation with *TRICERATOPS*

TRICERATOPS (Giacalone et al. 2021) is used to validate planet candidates using the Bayesian framework. The algorithm first starts searching for stars within a 2.″5 radius of the target star. It determines the contamination of the flux from these stars

Table 2
Details of High-resolution Imaging Data

TOI	Telescope	Instrument	Filter	Image Type	Contrast Δmag				
					0.″1	0.″5	1.″0	1.″5	2.″0
139	Gemini-N (8m)	‘Alopeke	562 nm	Speckle	3.849	4.104	4.450	…	…
	Gemini-N (8m)	‘Alopeke	832 nm	Speckle	4.383	6.372	7.354	…	…
	Keck II (10m)	NIRC2	BrGamma	AO	4.201	6.628	6.991	6.923	6.917
	Keck II (10m)	NIRC2	Jcont	AO	2.860	5.489	6.035	6.101	6.085
323	Gemini-N (8m)	‘Alopeke	562 nm	Speckle	3.807	4.285	4.372	…	…
	Gemini-N (8m)	‘Alopeke	832 nm	Speckle	4.369	5.234	5.558	…	…
	VLT (8m)	NaCo	Ks	AO	1.405	4.993	5.240	5.219	5.165
493	Gemini-N (8m)	NIRI	BrGamma	AO	1.491	4.929	6.946	…	…
	Keck II (10m)	NIRC2	BrGamma	AO	3.515	7.454	7.581	7.646	7.528
672	Gemini-S (8m)	Zorro	562 nm	Speckle	4.565	5.180	5.429	…	…
	Gemini-S (8m)	Zorro	832 nm	Speckle	4.784	6.182	7.494	…	…
815	Gemini-S (8m)	Zorro	562 nm	Speckle	5.206	6.354	6.925	…	…
	Gemini-S (8m)	Zorro	832 nm	Speckle	4.927	6.569	7.539	…	…
913	Gemini-S (8m)	Zorro	562 nm	Speckle	3.338	3.896	3.819	…	…
	Gemini-S (8m)	Zorro	832 nm	Speckle	4.868	6.472	7.132	…	…
1179	Gemini-N (8m)	‘Alopeke	562 nm	Speckle	3.701	4.419	4.541	…	…
	Gemini-N (8m)	‘Alopeke	832 nm	Speckle	4.832	6.683	7.606	…	…
1180	SAI (2.5m)	Speckle Polarimeter	I	Speckle	1.960	5.643	7.355	…	…
1694	Gemini-N (8m)	‘Alopeke	562 nm	Speckle	3.712	3.923	3.977	…	…
	Gemini-N (8m)	‘Alopeke	832 nm	Speckle	5.691	5.989	6.258	…	…
	Keck II (10m)	NIRC2	Ks	AO	3.854	6.482	6.545	6.504	6.459
1732	Palomar (5m)	PHARO	BrGamma	AO	2.592	6.768	8.216	8.275	8.250
	Gemini-N (8m)	‘Alopeke	562 nm	Speckle	4.134	4.467	4.509	…	…
	Gemini-N (8m)	‘Alopeke	832 nm	Speckle	5.008	6.554	7.399	…	…
	Shane (3m)	ShARCS	K	AO	0.613	2.836	4.481	5.482	6.408
2194	SOAR (4.1m)	HRCam	I	Speckle	2.118	4.831	5.437	5.931	6.423
2443	Gemini-N (8m)	‘Alopeke	562 nm	Speckle	5.219	5.729	5.952	…	…
	Gemini-N (8m)	‘Alopeke	832 nm	Speckle	5.389	6.943	8.223	…	…
	Palomar (5m)	PHARO	BrGamma	AO	2.351	6.697	7.910	8.753	9.146
2459	SOAR (4.1m)	HRCam	I	Speckle	2.134	5.321	5.807	6.186	6.578
3568	Keck II (10m)	NIRC2	Ks	AO	3.746	6.773	6.833	6.812	6.791
	Palomar (5m)	PHARO	BrGamma	AO	2.809	6.670	7.491	7.639	7.627
	Palomar (5m)	PHARO	Hcont	AO	2.273	6.898	8.135	8.414	8.462
3896	Palomar (5m)	PHARO	BrGamma	AO	2.585	6.908	7.893	8.101	8.128
3913	Palomar (5m)	PHARO	BrGamma	AO	2.289	6.551	7.520	7.635	7.726
4090	Palomar (5m)	PHARO	BrGamma	AO	1.724	6.929	7.958	8.235	8.263
4308	SOAR (4.1m)	HRCam	I	Speckle	2.143	4.405	5.053	5.602	6.156
5803	SOAR (4.1m)	HRCam	I	Speckle	1.921	3.766	4.039	4.272	4.510

to the TESS aperture. For the target star and other stars that seem to contribute enough to the transit signal, TRICERATOPS calculates the probability of that signal being generated by a transiting planet, an eclipsing binary, or a nearby eclipsing binary based on the measurements of marginal likelihood for each scenario. This is then combined with prior probability, based on which it calculates the final FPP and nearby FPP (NFPP). Mathematically it can be expressed as follows:

$$\begin{aligned} \mathrm{FPP} &= 1 - (\mathcal{P}_{\mathrm{TP}} + \mathcal{P}_{\mathrm{PTP}} + \mathcal{P}_{\mathrm{DTP}}) \\ \mathrm{NFPP} &= \Sigma(\mathcal{P}_{\mathrm{NTP}} + \mathcal{P}_{\mathrm{NEB}} + \mathcal{P}_{\mathrm{NEBX2P}}) \end{aligned} \quad (1)$$

where $\mathcal{P}_j$ shows probability of each scenarios that can be found on Table 1 of Giacalone et al. (2021; i.e., TP = no unresolved companion; transiting planet with Period around target star, PTP = unresolved bound companion; transiting planet with Period around primary star, DTP = unresolved background star; transiting planet with Period around target star, NTP = no unresolved companion; transiting planet with Period around nearby star, NEB = no unresolved companion; eclipsing binary with Period around nearby star and NEBX2P = no unresolved companion; eclipsing binary with 2×Period around nearby

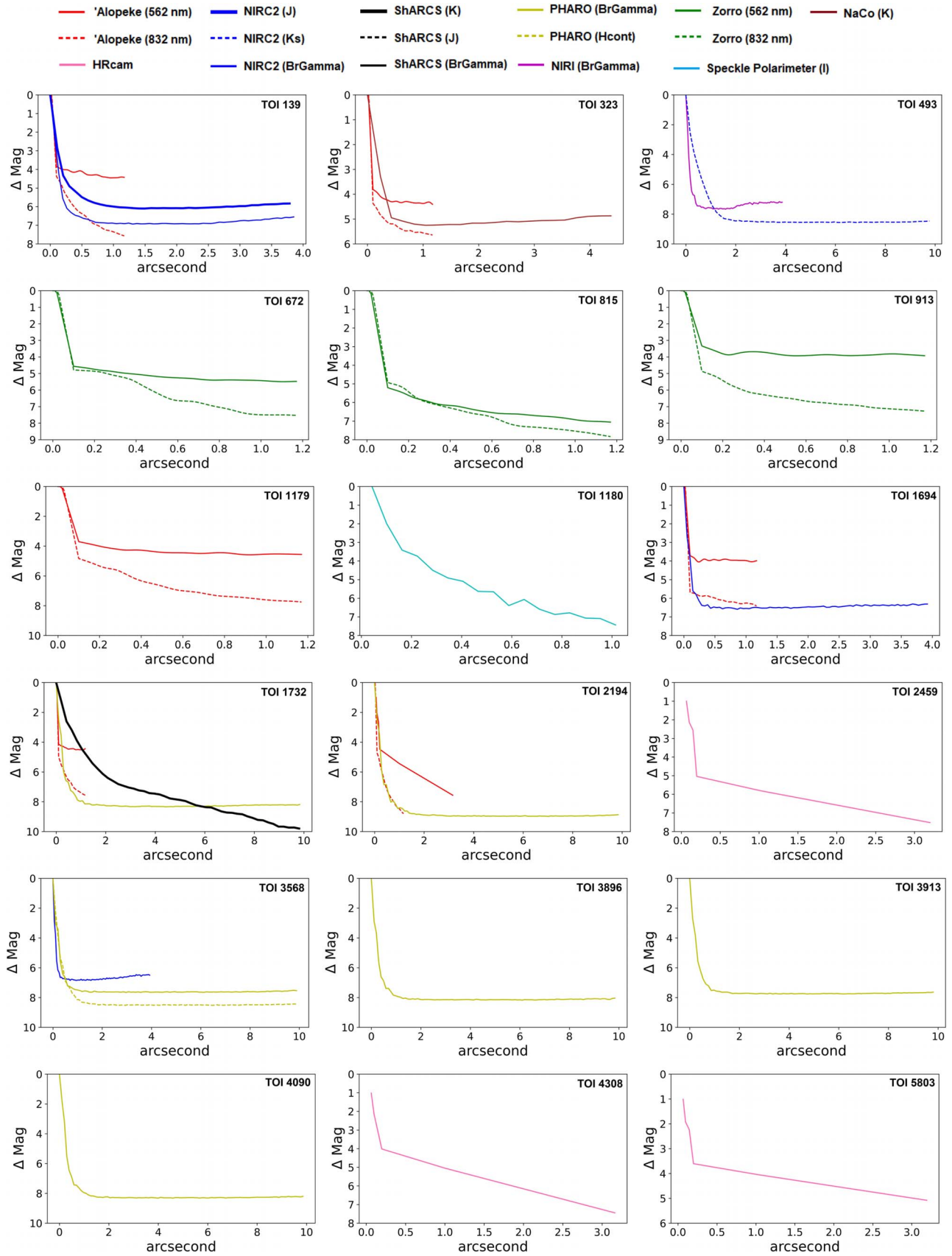

Figure 4. Contrast curves extracted from the high-resolution follow-up observations, which allows us to rule out companions at a given separation above a certain Δ Magnitude.

Table 3
Ground-based Light-curve Observations

Observatory	Ap (m)	Location	UTC Date	Filter	Result	Disp.[a]
TOI-139.01						
SLR2[b]-SAAO	0.5	Sutherland, S. Africa	2018-10-31	V	Possible NEB at 73″ (TIC 62482371)	CPC
LCOGT[c]-CTIO	1.0	Cerro Tololo, Chile	2019-07-24	Y[d]	Cleared all 5 NEB check stars, including the 73″ star	
[1.5mm] TOI-672.01						
LCOGT-CTIO	0.4	Cerro Tololo, Chile	2019-05-12	i'	∼9 ppt transit in 4″ target aperture	
Evans	0.36	El Sauce, Chile	2019-05-12	R_c	∼8 ppt egress in 7″ target aperture	
PEST[e]	0.3	Perth, Australia	2019-05-26	R_c	∼8 ppt transit in 7″ target aperture	VPC+
TRAPPIST-S	0.6	La Silla, Chile	2019-06-09	z'	∼8 ppt transit in 5″ target aperture	
Evans	0.36	El Sauce, Chile	2020-02-01	B	∼8 ppt transit in 6″ target aperture	
LCOGT-SSO	1.0	Siding Spring, Australia	2020-03-19	g'	∼8 ppt transit in 4″ target aperture	
TOI-913.01						
LCOGT-CTIO	1.0	Cerro Tololo, Chile	2020-03-05	z_s[g]	Tentative ∼1 ppt transit in 5″ target aper.	VPC
LCOGT-SAAO	1.0	Sutherland, S. Africa	2020-05-21	z_s	∼1.1 ppt transit in 5″ target aperture	
LCOGT-CTIO	1.0	Cerro Tololo, Chile	2021-05-12	z_s	Tentative ∼1 ppt transit in 5″ target aper.	
ASTEP[f]	0.4	Dome C, Antarctica	2022-09-12	R_c	Tentative $\sim 1-2$ ppt ingress in contaminated 11″ target aper.	
TOI-1694.01						
Catania Obs.	0.91	Catania, Italy	2020-02-16	R	∼4 ppt transit in 3″ target aperture	
Grand-Pra Obs.	0.4	Valais Sion, Switzerland	2020-12-10	g'	∼4 ppt egress in 6″ target aperture	VPC+
Dragonfly	1.0	Mayhill, NM, USA	2021-01-02	g', r'	∼5 ppt egress in <26″ target apertures	
TOI-2194.01						
LCOGT-SAAO	1.0	Sutherland, S. Africa	2021-07-09	Y	All seven NEB check stars cleared	CPC
LCOGT-CTIO	1.0	Cerro Tololo, Chile	2022-05-28	z_s	Tentative 700 ppm transit in 9″ target aper.	
TOI-2443.01						
LCOGT-SSO	1.0	Siding Spring, Australia	2021-09-19	Y	Cleared all three NEB check stars	CPC
TOI-2459.01						
LCOGT-CTIO	1.0	Cerro Tololo, Chile	2021-02-09	z_s	∼2 ppt ingress in 5″ target aperture	VPC
PEST	0.3	Perth, Australia	2021-11-03	g'	∼3 ppt transit in 8″ target aperture	
TOI-3082.01						
TRAPPIST-S	0.6	La Silla, Chile	2022-04-20	I+z'	∼2.5 ppt transit in 5″ target aperture	VPC+
LCOGT-McD	1.0	McDonald Obs, TX, USA	2022-05-16	i'	∼2.5 ppt transit in 4″ target aperture	
LCOGT-CTIO	1.0	Cerro Tololo, Chile	2022-05-16	i'	∼2.5 ppt transit in 4″ target aperture	
TCS-MuSCAT2[h]	1.52	Canaries, Spain	2022-05-21	g', r', i', z_s	∼2.5 ppt transits in 11″ target apertures (transit depths 1.5σ consistent across bands)	
TOI-4308.01						
-	…	…	…	…	No follow-up available	PC
TOI-5704.01						
LCOGT MuSCAT3	2.0	Haleakala, Hawaii	2023-01-24	g', r', i', z_s	tentative ∼1.5 ppt event in 7″ target apertures that are contaminated with 1.″5 neighbor TIC 900281091 ($\Delta T = 5.42$)	PC
TOI-5803.01						
-	…	…	…	…	No follow-up available	PC

Notes.
[a] The overall follow-up disposition. CPC = cleared of NEBs, VPC = on target relative to Gaia DR3 stars, VPC+ = achromatic on target relative to Gaia DR3 stars. See the text for full disposition definitions.
[b] Solaris network of telescopes of the Nicolaus Copernicus Astronomical Center of the Polish Academy of Sciences.
[c] Las Cumbres Observatory Global Telescope (LCOGT; Brown et al. 2013) 0.4 m, 1.0 m, 2.0 m network nodes at Cerro Tololo Inter-American Observatory (CTIO), South Africa Astronomical Observatory (SAAO), Siding Spring Observatory (SSO), McDonald Observatory (McD), and MuSCAT3 (Narita et al. 2020) on Faulkes Telescope North at Haleakala Observatory. Images calibrated by `BANZAI` pipeline (McCully et al. 2018) and photometry extracted using `AstroImageJ` (Collins et al. 2017).
[d] Pan-STARRS Y band ($\lambda_c = 10040$ Å, Width = 1120 Å)
[e] Perth Exoplanet Survey Telescope. Images calibrated and photometry extracted using `C-Munipack`[9] (see footnote) http://c-munipack.sourceforge.net.
[f] Antarctica Search for Transiting ExoPlanets (ASTEP; Guillot et al. (2015)): 0.4 m Newton Telescope installed at the Concordia station, Antarctica using a camera functioning in the R band (Schmider et al. 2020). Data reduction follows Mékarnia et al. (2016).
[g] Pan-STARRS z-short band ($\lambda_c = 8700$ Å, Width = 1040 Å).
[h] MuSCAT2 (Narita et al. 2019) 4-color multi-band simultaneous camera on the 1.52̃m Telescopio Carlos S\'anchez (TCS). Data reduction follows Parviainen et al. (2019).

Table 4
False-positive Probabilities of all the Targets Calculated using TRICERATOPS

TOI ID	TIC ID	S/N	FAP [%]	TRICERATOPS		CC File
				μ(FPP) $\pm$ σ(FPP)	μ(NFPP) $\pm$ σ(NFPP)	
				Validated Planets		
TOI 139.01	TIC 62483237					
	Sector 01	18.6619	0.01	$7.88 \times 10^{-04} \pm 4.88 \times 10^{-04}$	0.00 ± 0.00	'Alopeke (562 nm)
	Sector 28	15.0097	0.01	$9.03 \times 10^{-04} \pm 2.87 \times 10^{-04}$	0.00 ± 0.00	
	Sector 01			$2.25 \times 10^{-04} \pm 7.13 \times 10^{-05}$	0.00 ± 0.00	'Alopeke (832 nm)
	Sector 28			$3.05 \times 10^{-04} \pm 7.06 \times 10^{-05}$	0.00 ± 0.00	
	Sector 01			$3.12 \times 10^{-04} \pm 1.58 \times 10^{-04}$	0.00 ± 0.00	NIRC2 (BrGamma)
	Sector 28			$3.34 \times 10^{-04} \pm 2.16 \times 10^{-04}$	0.00 ± 0.00	
	Sector 01			$3.78 \times 10^{-04} \pm 1.99 \times 10^{-04}$	0.00 ± 0.00	NIRC2 (J)
	Sector 28			$8.44 \times 10^{-04} \pm 3.76 \times 10^{-04}$	0.00 ± 0.00	
TOI 672.01	151825527					
	Sector 09	43.1068	0.01	$7.34 \times 10^{-09} \pm 9.90 \times 10^{-09}$	$2.52 \times 10^{-13} \pm 2.63 \times 10^{-13}$	Zorro (562 nm)
	Sector 10	38.8176	0.01	$5.56 \times 10^{-07} \pm 2.00 \times 10^{-06}$	$5.14 \times 10^{-13} \pm 2.56 \times 10^{-13}$	
	Sector 36	41.0399	0.01	$9.12 \times 10^{-06} \pm 3.07 \times 10^{-05}$	$3.26 \times 10^{-46} \pm 1.84 \times 10^{-46}$	
	Sector 09			$2.01 \times 10^{-07} \pm 4.45 \times 10^{\dot{}}07$	$1.20 \times 10^{-13} \pm 6.99 \times 10^{-14}$	Zorro (832 nm)
	Sector 10			$2.42 \times 10^{-08} \pm 5.67 \times 10^{\dot{}}08$	$5.48 \times 10^{-13} \pm 2.62 \times 10^{-13}$	
	Sector 36			$6.76 \times 10^{-08} \pm 1.99 \times 10^{\dot{}}07$	$2.71 \times 10^{-46} \pm 1.68 \times 10^{-46}$	
TOI 913.01	407126408					
	Sector 12	15.6221	0.01	$4.01 \times 10^{-04} \pm 1.34 \times 10^{-04}$	$1.05 \times 10^{-26} \pm 4.40 \times 10^{-28}$	Zorro (562 nm)
	Sector 13	16.5437	0.01	$2.59 \times 10^{-03} \pm 4.95 \times 10^{-04}$	$1.82 \times 10^{-71} \pm 9.15 \times 10^{-73}$	
	Sector 12			$1.04 \times 10^{-04} \pm 3.71 \times 10^{-05}$	$1.11 \times 10^{-26} \pm 5.58 \times 10^{-28}$	Zorro (832 nm)
	Sector 13			$8.26 \times 10^{-04} \pm 2.04 \times 10^{-04}$	$1.90 \times 10^{-71} \pm 1.14 \times 10^{-72}$	
TOI 1694.01	396740648					
	Sector 19	49.3381	0.01	$1.76 \times 10^{-03} \pm 2.53 \times 10^{-03}$	0.00 ± 0.00	'Alopeke (562 nm)
	Sector 20	48.6979	0.01	$1.59 \times 10^{-03} \pm 2.52 \times 10^{-03}$	$5.26 \times 10^{-108} \pm 6.93 \times 10^{-108}$	
	Sector 19			$2.71 \times 10^{-03} \pm 3.24 \times 10^{-03}$	0.00 ± 0.00	'Alopeke (832 nm)
	Sector 20			$2.82 \times 10^{-03} \pm 3.74 \times 10^{-03}$	$6.73 \times 10^{-108} \pm 1.14 \times 10^{-107}$	
	Sector 19			$1.92 \times 10^{-05} \pm 4.58 \times 10^{-05}$	0.00 ± 0.00	NIRC2 (Ks)
	Sector 20			$8.93 \times 10^{-06} \pm 1.69 \times 10^{-05}$	$3.51 \times 10^{-108} \pm 5.77 \times 10^{-108}$	
TOI 2194.01	271478281					
	Sector 27	29.3712	0.01	$1.32 \times 10^{-06} \pm 3.88 \times 10^{-06}$	0.00 ± 0.00	HRCam (I)
TOI 2443.01	318753380					
	Sector 31	33.3454	0.01	$1.58 \times 10^{-17} \pm 8.24 \times 10^{-17}$	$1.97 \times 10^{-19} \pm 1.00 \times 10^{-19}$	'Alopeke (562 nm)
	Sector 31			$1.05 \times 10^{-13} \pm 3.95 \times 10^{-13}$	$2.28 \times 10^{-19} \pm 1.21 \times 10^{-19}$	'Alopeke (832 nm)
	Sector 31			$1.11 \times 10^{-11} \pm 3.55 \times 10^{-11}$	$1.50 \times 10^{-19} \pm 5.81 \times 10^{-20}$	PHARO (BrGamma)
TOI 2459.01	192790476					
	Sector 05			$8.52 \times 10^{-04} \pm 7.63 \times 10^{-05}$	$8.28 \times 10^{-04} \pm 6.07 \times 10^{-05}$	HRCam (I)
	Sector 06			$3.71 \times 10^{-04} \pm 2.03 \times 10^{-04}$	$2.56 \times 10^{-04} \pm 2.04 \times 10^{-05}$	
	Sector 32			$2.44 \times 10^{-06} \pm 6.22 \times 10^{-06}$	$1.44 \times 10^{-07} \pm 1.67 \times 10^{-08}$	
	Sector 33			$7.08 \times 10^{-04} \pm 6.01 \times 10^{-05}$	$6.98 \times 10^{-04} \pm 4.91 \times 10^{-05}$	
TOI 3082.01	428699140					
	Sector 37	16.8096	0.01	$6.78 \times 10^{-03} \pm 1.06 \times 10^{-03}$	$1.39 \times 10^{-27} \pm 1.06 \times 10^{-27}$	-
TOI 4308.01	144193715					
	Sector 01	8.9739	0.01	$5.98 \times 10^{-03} \pm 3.63 \times 10^{-04}$	$1.64 \times 10^{-10} \pm 2.40 \times 10^{-11}$	HRCam (I)
TOI 5704.01	148673433					
	Sector 22	18.0160	0.01	$8.56 \times 10^{-03} \pm 4.97 \times 10^{-05}$	$5.51 \times 10^{-04} \pm 1.49 \times 10^{-05}$	-
	Sector 48	16.8362	0.01	$6.61 \times 10^{-03} \pm 1.03 \times 10^{-03}$	$5.82 \times 10^{-06} \pm 5.28 \times 10^{-07}$	
TOI 5803.01	466382581					
	Sector 55	18.9821	0.01	$9.31 \times 10^{-03} \pm 2.74 \times 10^{-03}$	$4.54 \times 10^{-08} \pm 3.21 \times 10^{-09}$	HRCam (I)
				Likely Planets		
TOI 323	251852984					
	Sector 37	12.8622	0.01	$2.49 \times 10^{-01} \pm 2.30 \times 10^{-02}$	$3.20 \times 10^{-11} \pm 7.36 \times 10^{-12}$	'Alopeke (562 nm)
	Sector 37			$2.57 \times 10^{-01} \pm 2.75 \times 10^{-02}$	$3.59 \times 10^{-11} \pm 5.88 \times 10^{-12}$	'Alopeke (832 nm)
	Sector 37			$2.56 \times 10^{-01} \pm 2.09 \times 10^{-02}$	$2.78 \times 10^{-11} \pm 4.54 \times 10^{-12}$	NaCo (K)

Table 4
(Continued)

TOI ID	TIC ID	S/N	FAP [%]	TRICERATOPS		CC File
				μ(FPP) $\pm$ σ(FPP)	μ(NFPP) $\pm$ σ(NFPP)	
TOI 1180	158002130					
	Sector 14	17.9456	0.01	$7.99 \times 10^{-03} \pm 5.87 \times 10^{-04}$	$7.13 \times 10^{-04} \pm 2.59 \times 10^{-05}$	Speckle Polarimeter (I)
	Sector 19	19.8802	0.01	$6.56 \times 10^{-03} \pm 1.13 \times 10^{-03}$	$2.34 \times 10^{-04} \pm 1.67 \times 10^{-05}$	
	Sector 20	13.5258	0.01	$1.28 \times 10^{-02} \pm 1.48 \times 10^{-03}$	$4.39 \times 10^{-03} \pm 1.13 \times 10^{-04}$	
	Sector 21	13.9659	0.01	$1.30 \times 10^{-02} \pm 1.14 \times 10^{-03}$	$4.31 \times 10^{-03} \pm 1.15 \times 10^{-04}$	
	Sector 40	20.0742	0.01	$5.07 \times 10^{-03} \pm 1.15 \times 10^{-03}$	$1.71 \times 10^{-05} \pm 2.48 \times 10^{-06}$	
	Sector 41	11.1516	0.01	$4.87 \times 10^{-03} \pm 1.11 \times 10^{-03}$	$2.22 \times 10^{-05} \pm 3.03 \times 10^{-06}$	
	Sector 47	17.2377	0.01	$1.86 \times 10^{-02} \pm 2.32 \times 10^{-03}$	$9.15 \times 10^{-03} \pm 8.68 \times 10^{-04}$	
	Sector 48	17.6670	0.01	$3.99 \times 10^{-02} \pm 3.78 \times 10^{-03}$	$1.86 \times 10^{-02} \pm 1.40 \times 10^{-03}$	
TOI 2200	142105158					
	Sector 27	31.8576	0.01	$1.05 \times 10^{-01} \pm 5.56 \times 10^{-02}$	$1.15 \times 10^{-19} \pm 3.67 \times 10^{-10}$	-
	Sector 28	33.0523	0.01	$1.46 \times 10^{-01} \pm 5.07 \times 10^{-02}$	$2.01 \times 10^{-07} \pm 5.37 \times 10^{-08}$	
	Sector 29	35.2422	0.01	$6.15 \times 10^{-02} \pm 2.88 \times 10^{-02}$	$7.44 \times 10^{-12} \pm 2.17 \times 10^{-12}$	
	Sector 30	34.8712	0.01	$5.01 \times 10^{-01} \pm 9.29 \times 10^{-02}$	$2.95 \times 10^{-06} \pm 4.58 \times 10^{-08}$	
	Sector 31	33.0510	0.01	$5.85 \times 10^{-02} \pm 2.04 \times 10^{-02}$	$1.48 \times 10^{-10} \pm 4.34 \times 10^{-11}$	
	Sector 32	33.4764	0.01	$3.94 \times 10^{-02} \pm 2.08 \times 10^{-02}$	$2.83 \times 10^{-14} \pm 1.28 \times 10^{-14}$	
	Sector 33	34.5528	0.01	$4.82 \times 10^{-01} \pm 9.15 \times 10^{-02}$	$2.42 \times 10^{-05} \pm 4.74 \times 10^{-06}$	
	Sector 34	35.6292	0.01	$2.95 \times 10^{-01} \pm 6.65 \times 10^{-02}$	$5.68 \times 10^{-10} \pm 2.01 \times 10^{-10}$	
	Sector 36	33.9929	0.01	$3.52 \times 10^{-01} \pm 9.12 \times 10^{-02}$	$6.92 \times 10^{-05} \pm 9.69 \times 10^{-05}$	
	Sector 37	34.8538	0.01	$7.23 \times 10^{-02} \pm 2.41 \times 10^{-02}$	$5.37 \times 10^{-13} \pm 1.13 \times 10^{-13}$	
	Sector 38	34.9817	0.01	$1.13 \times 10^{-01} \pm 4.40 \times 10^{-02}$	$1.19 \times 10^{-10} \pm 3.36 \times 10^{-11}$	
	Sector 39	37.0436	0.01	$4.86 \times 10^{-01} \pm 1.21 \times 10^{-01}$	$1.01 \times 10^{-08} \pm 3.36 \times 10^{-09}$	
TOI 2408	67630845					
	Sector 30	19.5685	0.01	$1.75 \times 10^{-01} \pm 2.89 \times 10^{-02}$	0.00 ± 0.00	-
TOI 3913	155898758					
	Sector 49	16.1696	0.01	$6.16 \times 10^{-01} \pm 4.30 \times 10^{-02}$	0.00 ± 0.00	PHARO (BrGamma)
	Sector 50	14.5601	0.01	$5.63 \times 10^{-02} \pm 6.18 \times 10^{-03}$	0.00 ± 0.00	
				Not Validated		
TOI 493	19025965					
	Sector 34	9.4971	0.01	$1.75 \times 10^{-02} \pm 1.62 \times 10^{-03}$	$3.31 \times 10^{-03} \pm 5.99 \times 10^{-04}$	NIRI (BrGamma)
	Sector 44	14.7922	0.01	$1.41 \times 10^{-02} \pm 3.09 \times 10^{-03}$	$1.06 \times 10^{-02} \pm 2.51 \times 10^{-03}$	
	Sector 45	12.3651	0.01	$2.24 \times 10^{-02} \pm 3.61 \times 10^{-03}$	$1.88 \times 10^{-02} \pm 3.45 \times 10^{-03}$	
	Sector 46	9.7146	0.01	$2.83 \times 10^{-02} \pm 7.96 \times 10^{-03}$	$1.72 \times 10^{-02} \pm 7.69 \times 10^{-03}$	
	Sector 34			$1.23 \times 10^{-02} \pm 1.62 \times 10^{-03}$	$3.56 \times 10^{-03} \pm 6.47 \times 10^{-04}$	NIRC2 (BrGamma)
	Sector 44			$1.08 \times 10^{-02} \pm 2.07 \times 10^{-03}$	$1.00 \times 10^{-02} \pm 1.85 \times 10^{-03}$	
	Sector 45			$1.94 \times 10^{-02} \pm 4.41 \times 10^{-03}$	$1.87 \times 10^{-02} \pm 4.39 \times 10^{-03}$	
	Sector 46			$2.99 \times 10^{-02} \pm 9.54 \times 10^{-03}$	$2.28 \times 10^{-02} \pm 9.19 \times 10^{-03}$	
TOI 815	102840239					
	Sector 36	15.7674	1.00	$2.23 \times 10^{-03} \pm 1.32 \times 10^{-03}$	$1.87 \times 10^{-03} \pm 1.32 \times 10^{-03}$	Zorro (562 nm)
	Sector 36			$2.13 \times 10^{-03} \pm 1.32 \times 10^{-03}$	$1.77 \times 10^{-03} \pm 1.32 \times 10^{-03}$	Zorro (832 nm)
TOI 1179	148914726					
	Sector 14	41.5323	0.01	$9.98 \times 10^{-01} \pm 1.51 \times 10^{-03}$	$2.79 \times 10^{-02} \pm 9.85 \times 10^{-03}$	'Alopeke (562 nm)
	Sector 15	47.9257	0.01	$9.87 \times 10^{-01} \pm 6.69 \times 10^{-03}$	$7.11 \times 10^{-02} \pm 2.72 \times 10^{-02}$	
	Sector 21	49.6108	0.01	$9.72 \times 10^{-01} \pm 1.57 \times 10^{-02}$	$5.84 \times 10^{-02} \pm 2.29 \times 10^{-02}$	
	Sector 22	43.6678	0.01	$2.51 \times 10^{-02} \pm 5.48 \times 10^{-03}$	$4.08 \times 10^{-03} \pm 1.48 \times 10^{-03}$	
	Sector 41	42.6402	0.01	$1.56 \times 10^{-01} \pm 7.08 \times 10^{-02}$	$3.46 \times 10^{-02} \pm 2.20 \times 10^{-02}$	
	Sector 48	42.5446	0.01	$9.82 \times 10^{-01} \pm 7.00 \times 10^{-03}$	$1.20 \times 10^{-01} \pm 4.19 \times 10^{-02}$	
	Sector 14			$9.96 \times 10^{-01} \pm 4.87 \times 10^{-03}$	$2.78 \times 10^{-01} \pm 7.95 \times 10^{-03}$	'Alopeke (832 nm)
	Sector 15			$9.78 \times 10^{-01} \pm 1.98 \times 10^{-02}$	$9.48 \times 10^{-02} \pm 2.78 \times 10^{-02}$	
	Sector 21			$9.82 \times 10^{-01} \pm 1.02 \times 10^{-02}$	$7.31 \times 10^{-02} \pm 2.08 \times 10^{-02}$	
	Sector 22			$2.17 \times 10^{-02} \pm 6.25 \times 10^{-03}$	$4.69 \times 10^{-03} \pm 1.74 \times 10^{-03}$	
	Sector 41			$1.32 \times 10^{-01} \pm 9.88 \times 10^{-02}$	$4.59 \times 10^{-02} \pm 3.57 \times 10^{-02}$	
	Sector 48			$9.67 \times 10^{-01} \pm 2.17 \times 10^{-02}$	$1.67 \times 10^{-01} \pm 4.12 \times 10^{-02}$	
TOI 1732	470987100					
	Sector 20	10.6478	0.01	$8.10 \times 10^{-03} \pm 1.26 \times 10^{-04}$	$7.33 \times 10^{-03} \pm 1.37 \times 10^{-04}$	PHARO (BrGamma)
	Sector 47	12.6158	0.01	$2.45 \times 10^{-04} \pm 9.89 \times 10^{-06}$	$2.15 \times 10^{-04} \pm 6.56 \times 10^{-06}$	
	Sector 20			$1.02 \times 10^{-02} \pm 1.53 \times 10^{-04}$	$8.08 \times 10^{-03} \pm 1.46 \times 10^{-04}$	'Alopeke (562 nm)

Table 4
(Continued)

TOI ID	TIC ID	S/N	FAP [%]	TRICERATOPS		CC File
				μ(FPP) $\pm$ σ(FPP)	μ(NFPP) $\pm$ σ(NFPP)	
	Sector 47			$2.72 \times 10^{-04} \pm 1.46 \times 10^{-05}$	$3.37 \times 10^{-04} \pm 1.34 \times 10^{-05}$	
	Sector 20			$8.84 \times 10^{-03} \pm 2.44 \times 10^{-04}$	$8.26 \times 10^{-03} \pm 2.43 \times 10^{-04}$	'Alopeke (832 nm)
	Sector 47			$2.45 \times 10^{-04} \pm 1.01 \times 10^{-05}$	$2.34 \times 10^{-04} \pm 7.39 \times 10^{-06}$	
	Sector 20			$1.17 \times 10^{-02} \pm 1.64 \times 10^{-04}$	$6.97 \times 10^{-03} \pm 9.31 \times 10^{-05}$	ShARCS (K)
	Sector 47			$3.92 \times 10^{-04} \pm 2.86 \times 10^{-05}$	$2.07 \times 10^{-04} \pm 1.06 \times 10^{-05}$	
TOI 3568	160390955					
	Sector 55	21.0566	0.01	$1.17 \times 10^{-02} \pm 6.66 \times 10^{-03}$	$1.88 \times 10^{-03} \pm 3.82 \times 10^{-04}$	NIRC2 (K)
	Sector 55			$3.61 \times 10^{-02} \pm 1.07 \times 10^{-02}$	$2.22 \times 10^{-03} \pm 4.26 \times 10^{-04}$	PHARO (Hcont)
	Sector 55			$2.32 \times 10^{-03} \pm 3.36 \times 10^{-03}$	$2.09 \times 10^{-03} \pm 5.63 \times 10^{-04}$	PHARO (BrGamma)
TOI 3896	445837596					
	Sector 48	11.1953	0.01	$1.40 \times 10^{-02} \pm 8.42 \times 10^{-04}$	$1.04 \times 10^{-03} \pm 3.75 \times 10^{-05}$	PHARO (BrGamma)
TOI 4090	289373041					
	Sector 53	12.7536	0.01	$3.95 \times 10^{-02} \pm 4.76 \times 10^{-03}$	$2.51 \times 10^{-02} \pm 1.69 \times 10^{-03}$	PHARO (BrGamma)
	Sector 54	15.2323	0.01	$5.63 \times 10^{-02} \pm 6.18 \times 10^{-03}$	$2.82 \times 10^{-02} \pm 2.79 \times 10^{-03}$	
TOI 5584	29169215					
	Sector 21	13.8631	0.01	$1.91 \times 10^{-02} \pm 1.33 \times 10^{-03}$	$7.18 \times 10^{-03} \pm 4.19 \times 10^{-04}$	-
	Sector 47	7.0555	0.10	$1.81 \times 10^{-01} \pm 6.31 \times 10^{-03}$	$1.46 \times 10^{-01} \pm 5.59 \times 10^{-03}$	

Note. μ represents the mean value and σ represents the standard deviation in the values of FPP and NFPP. CC File depicts the name of the instrument (filter used) from which the high-resolution image was taken and the respective filters used. TRICERATOPS takes CC file one at a time so we calculated FPP and NFPP for each CC file separately. S/N = signal-to-noise ratio and FAP = false-alarm probability, calculated using transit least squares.

star), which can be calculated by

$$\mathcal{P}_j = \frac{p(S_j|D)}{\Sigma p(S_j|D)} \quad (2)$$

where $p(S_j|D) \propto p(S_j)p(D|S_j)$. $p(S_j)$ is the prior probability of each scenario and $p(D|S_j)$ is the marginal likelihood or Bayesian evidence.

It can also use high-resolution imaging follow-up observations to constrain the area of sky around the target where an unresolved companion star can exist. To calculate FPP and NFPP using TRICERATOPS we give following input parameters and files: orbital period in days, transit depth, data of transit photometry, cadence in days, name of filter used by high-resolution imaging, and data of contrast curve. We calculated FPP and NFPP for each selected target with 15 iterations and tabulated the mean and standard deviation values in Table 4.

5. Validated Planets

We consider planetary candidates with high-resolution imaging showing no evidence of stellar companion and TRICERATOPS FPP of $<1.5 \times 10^{-2}$ and NFPP of $<10^{-3}$ (Giacalone et al. 2021) to be statistically validated. TRICERATOPS undertakes the nearby stars (within 2.″5 radius from the target) for which measured transit depths are nonzero to calculate the NFPP. In Appendix, we have compiled a list of such nearby stars that were considered by TRICERATOPS for calculating the NFPP for all of our validated planets. The tabulated probability clearly suggests that these stars are not contaminating our target star and thereby strongly suggesting that the transit source detected is originating solely from the target star. By examining the 24 candidates we validated 11 planetary systems. The properties of the new planets are shown in the top panel and the properties of new host stars are shown in the bottom panel of Figure 5. Our newly validated planets range in size from the super-Earth sized TOI-2194b (1.99 $R_\oplus$) to the sub-Saturn sized TOI-672b (5.26 $R_\oplus$) and TOI-1694b (5.46 $R_\oplus$). The derived planetary and orbital parameters for all 11 planets are listed in Table 5. Phase-folded transit light curves with the best-fit Juliet model are shown in Figure 6.

In this section we will discuss some of the interesting features of new systems. By using an unbiased mass–radius empirical relationship (Chen & Kipping 2017), which was developed upon the probabilistic mass–radius relation condition on a sample of known exoplanets and late-type stars, we approximated the mass of the newly validated planets. It is to be noted here that these mass estimates should not be considered robust for characterization of the planets properties, we used these estimates to get better idea of these systems. Based on this mass estimates we also calculated the semiamplitude of radial velocity that is induced on the host star by the orbiting planet. In order to facilitate the identification of the most optimal targets for atmospheric characterization among the TESS planet candidates, Kempton et al. (2018) developed a method for calculating transmission spectroscopy metrics (TSM) that is proportional to the expected transmission spectroscopy S/N, based on the strength of spectral features and the brightness of the host star, assuming cloud-free atmospheres and Emission Spectroscopy Metrics (ESM) that is proportional to the expected S/N of a JWST secondary eclipse detection at mid-IR wavelengths. The calculated TSM and ESM values for the candidates are tabulated in Table 6. This method allows for efficient prioritization of the most promising candidates for further study and characterization of their atmospheric properties.

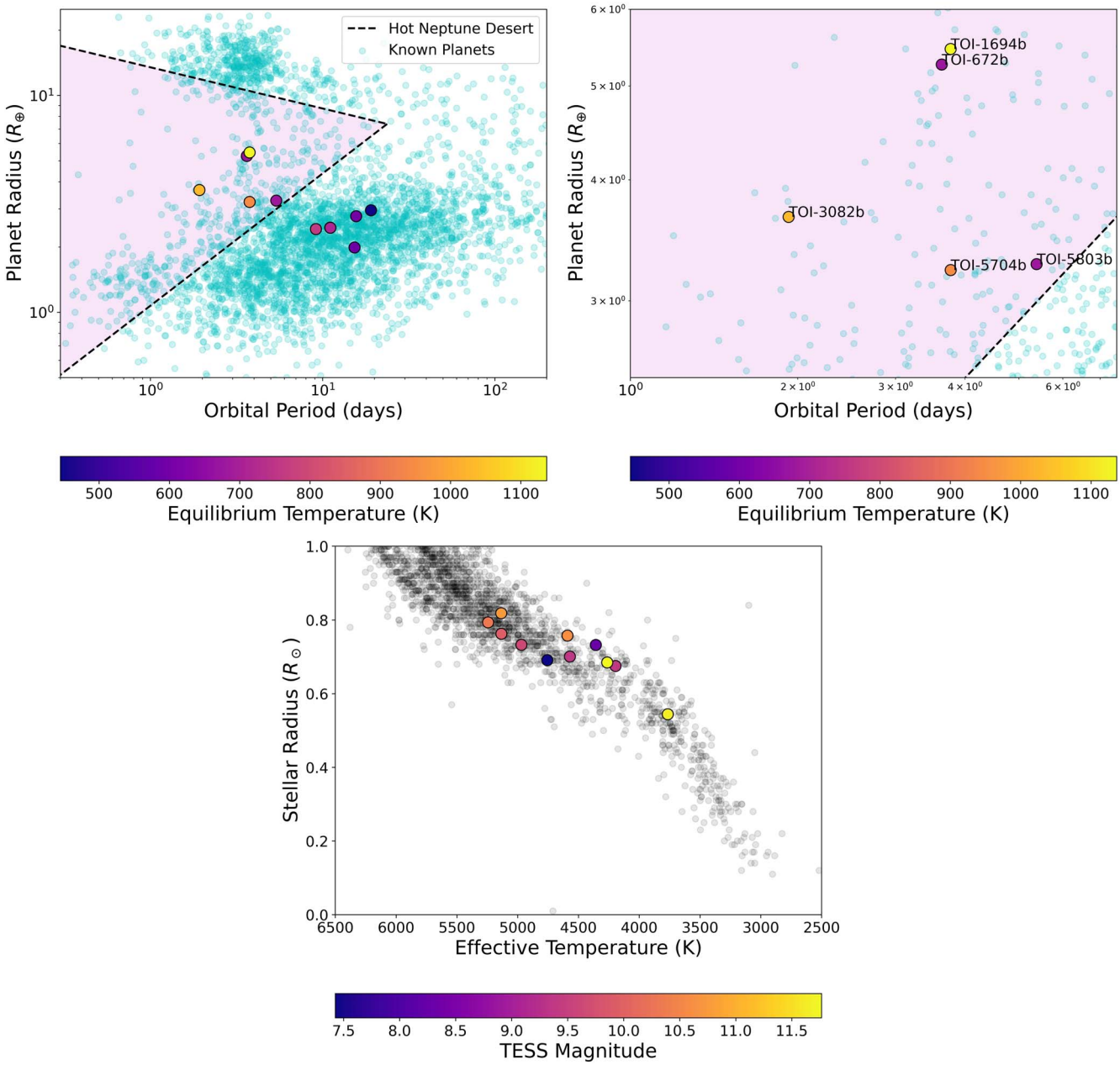

Figure 5. Properties of newly validated systems. Top panel: new planets and their comparison with previously known planets (with < 100 day period), shaded region depicts the hot-Neptune desert, figure in right panel is a zoomed-in version of the left figure with labels for the planets in the hot-Neptune desert. Five of the planets lie in the hot-Neptune desert. Right panel: new host stars compared to hosts of known planets. Data for these plots were taken from the NASA Exoplanet Archive.

Distribution of TSM and ESM for planets is shown in Figure 7. Using radial velocity mass measurements, it is recommended to quickly measure the original mass and follow up on targets that meet the suggested threshold values for these measurements.

5.1. TOI-139

TOI-139b is a sub-Neptune (2.4566 $R_\oplus$) planet orbiting bright (Vmag = 10.55, Tmag = 9.36) star TOI-139 (0.70 $R_\odot$, 0.69 $M_\odot$), observed in TESS sectors 1 and 28. It orbits the star at a distance of 0.11 au with an orbital period 11.07 days and having an equilibrium temperature 561.17 K. 'Alopeke and NIRC2 high-resolution imaging showed no contaminating stellar companion and ground-based follow-up observations have ruled out NEBs in all nearby (≈2.″5) Gaia DR2 and TIC stars that are bright enough to have caused the TESS detection. The TRICERATOPS FPP and NFPP are listed in Table 4 calculated using four available contrast curve files. These FPP values are consistent with the source of transit signal being on the target star. Using the Chen & Kipping (2017) mass–radius relationship we predicted the mass 6.8 ± 3.0 $M_\oplus$. Based on this, the resultant RV semiamplitude is 2.43 m s^{-1}. TSM and ESM are estimated as 68.30 and 3.18, respectively, which are below the recommended threshold of Kempton et al. (2018). So this target will not be favorable for either transmission or emission spectroscopy.

5.2. TOI-672

TOI-672b is a sub-Saturn or super-Neptune (5.26 $R_\oplus$) planet orbiting faint (Vmag = 13.57, Tmag = 11.67) star TOI-672 (0.54 $R_\odot$, 0.53 $M_\odot$), observed in TESS sectors 9, 10, and 36. It orbits the star at a distance of 0.039 au with an orbital period

Figure 6. Phase-folded light curves of newly validated planetary systems. The black line shows the best-fit model, blue dots are binned observations.

3.63 days and having an equilibrium temperature 676.15 K. Zorro high-resolution imaging showed no contaminating stellar companion, and ground-based follow-up observations verified the transit event occur within the target star follow-up aperture. There is no strong filter dependent depth chromaticity, and there are no other obvious or Gaia DR2 or TIC stars contaminating the follow-up aperture that are bright enough to cause the TESS detection. The `TRICERATOPS` FPP and NFPP are listed in Table 4 calculated using two available contrast curve files. These FPP values are consistent with the

Table 5
Planetary and Orbital Parameters for the Newly Validated Planetary Systems using Juliet

Planet	TIC ID	Period (days)	Epoch Time (BJD)	R_p/R_s	R_p ($R_\oplus$)	b	a/R_s	i (degree)
TOI-139b	62483237	$11.070850^{+0.000024}_{-0.000030}$	$2458334.8906^{+0.0010}_{-0.0010}$	$0.0321^{+0.0028}_{-0.0016}$	$2.4566^{+0.2122}_{-0.1245}$	$0.395^{+0.254}_{-0.252}$	$33.159^{+2.667}_{-5.336}$	$89.32^{+0.45}_{-0.65}$
TOI-672b	151825527	$3.633575^{+0.000001}_{-0.000001}$	$2458546.4799^{+0.0002}_{-0.0002}$	$0.0885^{+0.0014}_{-0.0017}$	$5.2604^{+0.0827}_{-0.0985}$	$0.424^{+0.108}_{-0.206}$	$15.503^{+1.055}_{-0.934}$	$88.43^{+0.82}_{-0.52}$
TOI-913b	407126408	$11.098644^{+0.000587}_{-0.000581}$	$2458625.2133^{+0.0024}_{-0.0023}$	$0.0306^{+0.0016}_{-0.0013}$	$2.4528^{+0.1269}_{-0.1009}$	$0.387^{+0.248}_{-0.254}$	$24.352^{+1.910}_{-3.825}$	$89.10^{+0.61}_{-0.87}$
TOI-1694b	396740648	$3.770179^{+0.000058}_{-0.000060}$	$2458817.2662^{+0.0004}_{-0.0007}$	$0.0610^{+0.0017}_{-0.0013}$	$5.4585^{+0.4682}_{-0.7919}$	$0.326^{+0.172}_{-0.198}$	$10.206^{+0.468}_{-0.792}$	$88.17^{+1.15}_{-1.19}$
TOI-2194b	271478281	$15.337597^{+0.001585}_{-0.001616}$	$2459037.3678^{+0.0013}_{-0.0011}$	$0.0263^{+0.0017}_{-0.0009}$	$1.9892^{+0.1313}_{-0.0668}$	$0.412^{+0.288}_{-0.253}$	$32.393^{+2.718}_{-6.864}$	$89.27^{+0.47}_{-0.85}$
TOI-2443b	318753380	$15.669494^{+0.000926}_{-0.001004}$	$2459148.0988^{+0.0007}_{-0.0007}$	$0.0347^{+0.0006}_{-0.0006}$	$2.7731^{+0.0493}_{-0.0515}$	$0.285^{+0.183}_{-0.175}$	$26.293^{+0.952}_{-2.053}$	$89.38^{+0.39}_{-0.48}$
TOI-2459b	192790476	$19.104718^{+0.000023}_{-0.000024}$	$2458452.3342^{+0.0007}_{-0.0007}$	$0.0400^{+0.0012}_{-0.0009}$	$2.9531^{+0.0916}_{-0.0658}$	$0.321^{+0.242}_{-0.209}$	$44.432^{+2.039}_{-5.404}$	$89.59^{+0.28}_{-0.41}$
TOI-3082b	428699140	$1.926907^{+0.000128}_{-0.000134}$	$2459309.1199^{+0.0010}_{-0.0010}$	$0.0489^{+0.0020}_{-0.0019}$	$3.6621^{+0.1464}_{-0.1448}$	$0.355^{+0.247}_{-0.223}$	$8.519^{+0.600}_{-1.286}$	$87.63^{+1.54}_{-2.39}$
TOI-4308b	144193715	$9.151201^{+0.000036}_{-0.000037}$	$2458333.4284^{+0.0026}_{-0.0029}$	$0.0279^{+0.0014}_{-0.0015}$	$2.4189^{+0.1195}_{-0.1333}$	$0.384^{+0.259}_{-0.253}$	$23.606^{+2.227}_{-3.906}$	$89.07^{+0.64}_{-0.92}$
TOI-5704b	148673433	$3.771116^{+0.0000115}_{-0.0000107}$	$2459610.7568^{+0.0008}_{-0.0007}$	$0.0389^{+0.0023}_{-0.0017}$	$3.2274^{+0.1873}_{-0.1398}$	$0.424^{+0.223}_{-0.272}$	$11.695^{+1.048}_{-2.486}$	$88.94^{+1.37}_{-2.29}$
TOI-5803b	466382581	$5.383050^{+0.000207}_{-0.000200}$	$2459802.7103^{+0.0004}_{-0.0005}$	$0.0393^{+0.0015}_{-0.0014}$	$3.2732^{+0.1251}_{-0.1194}$	$0.349^{+0.223}_{-0.233}$	$28.596^{+1.887}_{-3.423}$	$89.30^{+0.48}_{-0.60}$

Table 6
Estimated Parameters, TSM, and ESM for Newly Validated Planetary Systems

Planet	TIC ID	T_{eq} (K)	M_p ($M_\oplus$)	Density (cgs)	K m s^{-1}	TSM	ESM
TOI-139b	62483237	561.17	6.8 ± 3.0	2.45	2.4305	68.30	3.18
TOI-672b	151825527	676.15	24.2 ± 10.7	0.91	15.1375	134.15	22.93
TOI-913b	407126408	712.01	6.8 ± 2.9	2.46	2.1586	63.70	3.96
TOI-1694b	396740648	1136.57	25.5 ± 11.9	0.87	11.8096	125.91	25.89
TOI-2194b	271478281	590.88	4.9 ± 2.0	3.23	1.4536	131.02	5.45
TOI-2443b	318753380	600.83	8.3 ± 3.6	2.09	2.7401	132.89	8.28
TOI-2459b	192790476	445.01	9.1 ± 4.0	1.93	2.8544	76.04	2.46
TOI-3082b	428699140	1032.78	13.2 ± 5.8	1.46	8.7974	78.37	13.96
TOI-4308b	144193715	763.05	6.5 ± 2.7	2.50	2.1129	39.68	2.47
TOI-5704b	148673433	949.07	9.49 ± 4.4	1.55	5.3273	76.99	10.04
TOI-5803b	466382581	678.87	10.8 ± 4.8	1.69	4.3137	69.69	4.55

source of transit signal being on the target star. We can neglect the very low-probability NFPP scenarios because ground-based observations have confirmed the transit event on the target. Using the Chen & Kipping (2017) mass–radius relationship we predicted the mass $24.2 \pm 10.7\ M_\oplus$. Based on this, the resultant RV semiamplitude is 15.14 m s^{-1}. TSM and ESM are estimated as 134.15 and 22.93, respectively, which are above the recommended threshold of Kempton et al. (2018). So this target will be favorable for both transmission and emission spectroscopy.

5.3. TOI-913

TOI-913b is a sub-Neptune ($2.45\ R_\oplus$) planet orbiting bright (Vmag = 10.45, Tmag = 9.62) star TOI-913 ($0.73\ R_\odot$, $0.82\ M_\odot$), observed in TESS sectors 12 and 13. It orbits the star at a distance of 0.083 au with an orbital period 11.09 days and having an equilibrium temperature 712 K. Zorro high-resolution imaging showed no contaminating stellar companion and the ground-based follow-up observations verified the transit event occur within the target star follow-up aperture and that there are no other obvious or Gaia DR2 stars contaminating the follow-up aperture that are bright enough to cause the TESS detection. The `TRICERATOPS` FPP and NFPP are listed in Table 4 calculated using two available contrast curve files. These FPP values are consistent with the source of transit signal being on the target star. We can neglect the very low-probability NFPP scenarios because ground-based observations have confirmed the transit event on the target. Using the Chen & Kipping (2017) mass–radius relationship we predicted the mass $6.8 \pm 2.9\ M_\oplus$. Based on this, the resultant RV semiamplitude is 2.16 m s^{-1}. TSM and ESM are estimated as 63.71 and 3.96, respectively, which are below the recommended threshold of Kempton et al. (2018). So this target will not be favorable for either transmission or emission spectroscopy.

5.4. TOI-1694

TOI-1694b is a sub-Saturn or super-Neptune ($5.46\ R_\oplus$) planet orbiting bright (Vmag = 11.45, Tmag = 10.74) star TOI-1694 ($0.82\ R_\odot$, $0.84\ M_\odot$), observed in TESS sectors 19 and 20. It orbits the star at a distance of 0.039 au with an orbital period 3.77 days and having an equilibrium temperature 1136.57 K. 'Alopeke and NIRC2 high-resolution imaging showed no contaminating stellar companion and the ground-based follow-up observations verified the transit event occur within the target star follow-up aperture. There is no strong filter dependent depth chromaticity, and there are no other obvious or Gaia DR2 or TIC stars contaminating the follow-up aperture that are bright enough to cause the TESS detection. The `TRICERATOPS` FPP and NFPP are listed in Table 4 calculated using three available contrast curve files. These FPP values are consistent with the source of transit signal being on the target star. Using the Chen & Kipping (2017) mass–radius relationship we predicted the mass $25.5 \pm 11.9\ M_\oplus$. Based on this, the resultant RV semiamplitude is 11.81 m s^{-1}. TSM and ESM are

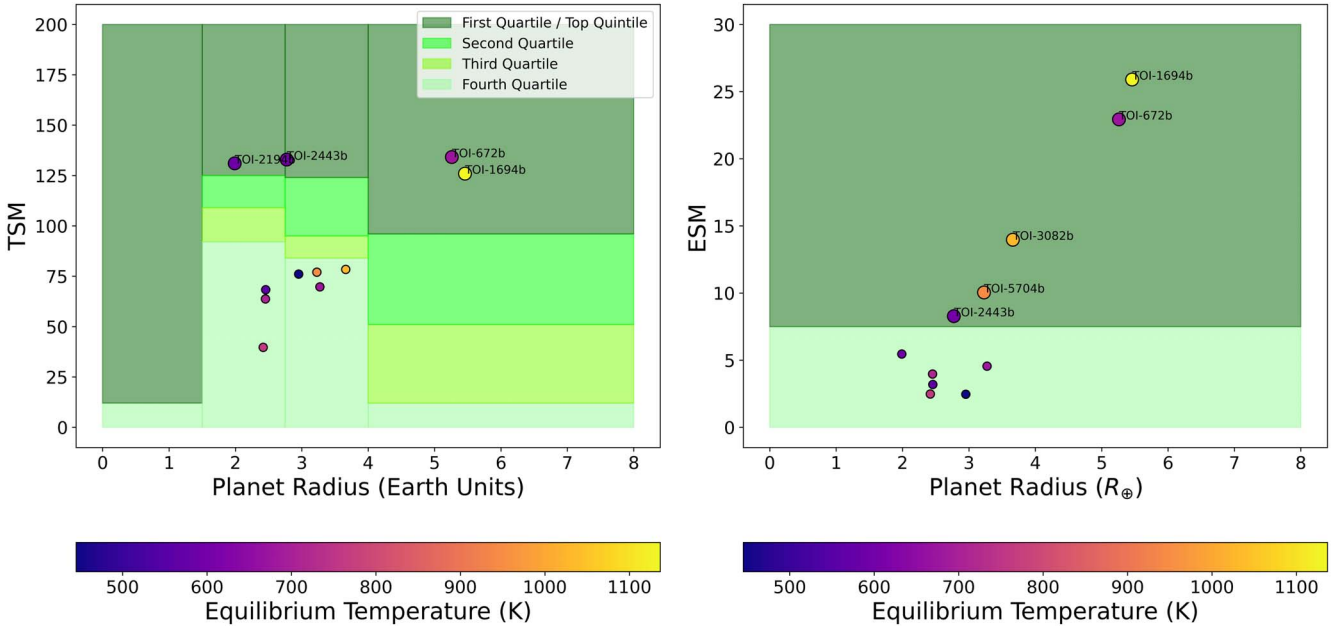

Figure 7. Transmission spectroscopy values (left) and emission spectroscopy values (right) for the newly validated planets, color-coded by their equilibrium temperature. In each case the shaded regions indicate areas of interest (dark green region) as identified by Kempton et al. (2018). Big dots represent the planets amenable for transmission or emission spectroscopy.

estimated as 125.91 and 25.89, respectively, which are above the recommended threshold of Kempton et al. (2018). So this target will be favorable for both transmission and emission spectroscopy. This planet also has one Jupiter analog outer companion TOI-1694c ($M \sin i = 1.05\ M_J$, P = 389 days) discovered by Van Zandt et al. (2023). Our predicted mass $25.5 \pm 11.9\ M_\oplus$ for TOI-1694b using Chen & Kipping (2017) is also comparable to the true measured by Van Zandt et al. (2023), which is $26.1 \pm 2.2\ M_\oplus$.

5.5. TOI-2194

TOI-2194b is a super-Earth ($1.99\ R_\oplus$) planet orbiting bright (*V*mag = 8.42, *T*mag = 7.42), metal-poor ([Fw/H] = -0.3720 ± 0.1) star TOI-2194 ($0.69\ R_\odot$, $0.74\ M_\odot$), observed in TESS sector 27. It orbits the star at a distance of 0.10 au with an orbital period 15.34 days and having an equilibrium temperature 590.88 K. HRCam high-resolution imaging showed no contaminating stellar companion and the ground-based follow-up observations have ruled out NEBs in all nearby ($\approx 2\farcs5$) Gaia DR2 and TIC stars that are bright enough to have caused the TESS detection. The TRICERATOPS FPP and NFPP are listed in Table 4 calculated using one available contrast curve file. These FPP values are consistent with the source of transit signal being on the target star. Using the Chen & Kipping (2017) mass–radius relationship we predicted the mass $4.9 \pm 2.0\ M_\oplus$. Based on this, the resultant RV semiamplitude is $1.45\ \mathrm{m\ s^{-1}}$. TSM is estimated as 131.023, which is above the threshold of second quartile suggested by Kempton et al. (2018); this makes it a good target for transmission spectroscopy. On the other hand ESM is 5.45, which is comparable but still below 7.5. So emission spectroscopy would be challenging.

5.6. TOI-2443

TOI-2443b is a sub-Neptune ($2.77\ R_\oplus$) planet orbiting bright (*V*mag = 9.51, *T*mag = 8.29) star TOI-2443 ($0.73\ R_\odot$, $0.66\ M_\odot$), observed in TESS sector 31. It orbits the star at a distance of 0.089 au with an orbital period 15.67 days and having an equilibrium temperature 600.83 K. This is the coolest planet validated in this project. 'Alopeke and PHARO high-resolution imaging showed no contaminating stellar companion and the ground-based follow-up observations have ruled out NEBs in all nearby ($\approx 2\farcs5$) Gaia DR2 and TIC stars that are bright enough to have caused the TESS detection. The TRICERATOPS FPP and NFPP are listed in Table 4 calculated using three available contrast curve files. These FPP values are consistent with the source of transit signal being on the target star. We can neglect the very low-probability NFPP scenarios because ground-based observations have confirmed the transit event on the target. Using the Chen & Kipping (2017) mass–radius relationship we predicted the mass $8.3 \pm 3.6\ M_\oplus$. Based on this, the resultant RV semiamplitude is $2.74\ \mathrm{m\ s^{-1}}$. TSM and ESM are estimated as 132.89 and 8.28, respectively, which are above the recommended threshold of Kempton et al. (2018). So this target will be favorable for both transmission and emission spectroscopy.

5.7. TOI-2459

TOI-2459b is a sub-Neptune ($2.95\ R_\oplus$) planet orbiting bright (*V*mag = 10.77, *T*mag = 9.39) star TOI-2459 ($0.67\ R_\odot$, $0.66\ M_\odot$), observed in TESS sectors 5, 6, 32, and 33. It orbits the star at a distance of 0.14 au with an orbital period 19.10 days and having an equilibrium temperature 445 K. High-resolution imaging showed no contaminating stellar companion and the ground-based follow-up observations verified the transit event occur within the target star follow-up aperture and that there are no other obvious or Gaia DR2 stars contaminating the follow-up aperture that are bright enough to cause the TESS detection. The TRICERATOPS FPP and NFPP are listed in Table 4, calculated using one available contrast curve file. These FPP values are consistent with the source of transit signal being on the target star. We can neglect the very low-probability NFPP scenarios because ground-based observations have confirmed

the transit event on the target. Using the Chen & Kipping (2017) mass–radius relationship we predicted the mass $9.1 \pm 4.0\ M_{\oplus}$. Based on this, the resultant RV semiamplitude is 2.85 m s^{-1}. TSM and ESM are estimated as 76.04 and 2.46, respectively, which are below the recommended threshold of Kempton et al. (2018). So this target will not be favorable for either transmission or emission spectroscopy.

5.8. TOI-3082

TOI-3082b is a Neptune-like (3.66 $R_{\oplus}$) planet orbiting faint (Vmag = 12.93, Tmag = 11.77) star TOI-3082 (0.68 $R_{\odot}$, 0.66 $M_{\odot}$), observed in TESS sectors 37. It orbits the star at a distance of 0.027 au with an orbital period 1.93 days and having an equilibrium temperature 1032.78 K. Ground-based follow-up observations verified the transit event occur within the target star follow-up aperture. There is no strong filter dependent depth chromaticity, and there are no other obvious or Gaia DR2 or TIC stars contaminating the follow-up aperture that are bright enough to cause the TESS detection. The TRICERATOPS FPP and NFPP are listed in Table 4 calculated without using any contrast curve file. These FPP values are consistent with the source of transit signal being on the target star. We can neglect the very low-probability NFPP scenarios because ground-based observations have confirmed the transit event on the target. Using the Chen & Kipping (2017) mass–radius relationship we predicted the mass $13.2 \pm 5.8\ M_{\oplus}$. Based on this, the resultant RV semiamplitude is 8.79 m s^{-1}. TSM is estimated as 78.37, which is below the threshold set by Kempton et al. (2018). However ESM is predicted to be 13.37 above the 7.5, indicating that it is potentially a good target for emission spectroscopy.

5.9. TOI-4308

TOI-4308b is a sub-Neptune (2.42 $R_{\oplus}$) planet orbiting bright (Vmag = 11.25, Tmag = 10.34) star TOI-4608 (0.79 $R_{\odot}$, 0.9 $M_{\odot}$), observed in TESS sector 1. It orbits the star at a distance of 0.087 au with an orbital period 9.15 days and having an equilibrium temperature 763.05 K. HRCam high-resolution imaging showed no contaminating stellar companion. The TRICERATOPS FPP and NFPP are listed in Table 4 calculated using one available contrast curve file. These FPP values are consistent with the source of transit signal being on the target star. Using the Chen & Kipping (2017) mass–radius relationship we predicted the mass $6.5 \pm 2.7\ M_{\oplus}$. Based on this, the resultant RV semiamplitude is 2.11 m s^{-1}. TSM and ESM are estimated as 39.68 and 2.48, respectively, which are below the recommended threshold of Kempton et al. (2018). So this target will not be favorable for either transmission or emission spectroscopy.

5.10. TOI-5704

TOI-5704b is a sub-Neptune (3.23 $R_{\oplus}$) planet orbiting bright (Vmag = 11.529, Tmag = 10.6147) star TOI-5704 (0.76 $R_{\odot}$, 0.73 $M_{\odot}$), observed in TESS sectors 22 and 48. It orbits the star at a distance of 0.04 au with an orbital period 3.77 days and having an equilibrium temperature 949.07 K. Ground-based follow-up observation found the transit event in 7″ target apertures that are contaminated with 1.5″ neighbor TIC 900281091. We calculated the probability of the signal originating from the contaminating star, which was found to be 1.79×10^{-10} (see Table 7), thus ruling out the possibility of contamination. The TRICERATOPS FPP and NFPP are listed in Table 4 calculated without using any contrast curve file. These FPP values are consistent with the source of transit signal being on the target star. Using the Chen & Kipping (2017) mass–radius relationship we predicted the mass $9.49 \pm 4.4\ M_{\oplus}$. Based on this, the resultant RV semiamplitude is 5.33 m s^{-1}. TSM is estimated as 76.99, which is comparable but still below the threshold set by Kempton et al. (2018). However ESM is predicted to be 10.04 above the 7.5, indicating that it is potentially a good target for emission spectroscopy.

5.11. TOI-5803

TOI-5803b is a sub-Neptune (3.27 $R_{\oplus}$) planet orbiting bright (Vmag = 10.65, Tmag = 9.94) star TOI-5803 (0.76 $R_{\odot}$, 0.87 $M_{\odot}$), observed in TESS sector 55. It orbits the star at a distance of 0.10 au with an orbital period 5.38 days and having an equilibrium temperature 678.87 K. HRCam high-resolution imaging showed no contaminating stellar companion. The TRICERATOPS FPP and NFPP are listed in Table 4 calculated using one available contrast curve file. TRICERATOPS has observed one nearby star TIC 2025175669 at the separation of 6.″82 with $\Delta mag = 7$, but the further calculation using TRICERATOPS found out that this target has nonzero transit depth so it eventually ruled out the possibility of any contamination. These FPP values are consistent with the source of transit signal being on the target star. Using the Chen & Kipping (2017) mass–radius relationship we predicted the mass $10.8 \pm 4.8\ M_{\oplus}$. Based on this, the resultant RV semiamplitude is 4.31 m s^{-1}. TSM and ESM are estimated as 69.70 and 4.55, respectively, which are below the recommended threshold of Kempton et al. (2018). So this target will not be favorable for either transmission or emission spectroscopy.

6. Likely Planets and Not Validated Candidates

In Table 4, we have listed the likely planets along with the not validated candidates. In the case of TRICERATOPS, the target would be classified as a "likely planet" if FPP is <0.5 and NFPP is $<10^{-03}$ and "likely false positive" if NFPP $>10^{-03}$ (Giacalone et al. 2021). We have identified five likely planet targets that can be further followed up to establish their planetary nature. These targets are TOI-323, TOI-1180, TOI-2200, TOI-2408, and TOI-3913. The targets remain unvalidated due to not passing the TRICERATOPS threshold are TOI-493, TOI 815 (noisy signal with 1% false-alarm probability), TOI 1179 (TRICERATOPS has detected blended eclipsing binary), TOI 1732 (FPP for sector 47 passed the validation threshold but sector 20 showing FPP above the threshold), TOI-3568, TOI-3896, TOI-4090, and TOI-5584.

7. Conclusions

Using ground-based light curves, high-resolution imaging, and the statistical validation tool TRICERATOPS, out of the 24 initial candidates selected for examination, 11 new TESS exoplanetary systems have been statistically validated. Among these recently validated planets, there are several intriguing targets that worthy for further investigation into their atmospheres. For example, based on the estimated TSM values, TOI-2194b is considered a promising candidate for the investigation of its atmosphere via transmission spectroscopy.

Similarly, TOI-3082b and TOI-5704b are considered to be optimal targets for investigating via emission spectroscopy, as per their estimated ESM values. Additionally, based on the TSM and ESM values, TOI-672b, TOI-1694b, and TOI-2443b are considered to be promising candidates for the investigation of their atmospheres via both transmission and emission spectroscopy. Furthermore, we have identified five potential planets that would benefit from further investigation through the use of radial velocity and high-resolution imaging techniques in order to establish their planetary nature with a high degree of certainty. These investigations would help to reveal more about the properties and behavior of these exoplanets and provide insights into the formation and evolution of planetary systems.

M.V.G. and I.A.S. acknowledge the support of Ministry of Science and Higher Education of the Russian Federation under the grant 075-15-2020-780 (N13.1902.21.0039). Funding for the TESS mission is provided by NASA's Science Mission Directorate. KAC acknowledges support from the TESS mission via subaward s3449 from MIT. Some of the observations in this paper made use of the High-Resolution Imaging instruments 'Alopeke and Zorro and were obtained under Gemini LLP Proposal Number: GN/S-2021A-LP-105. 'Alopeke and Zorro were funded by the NASA Exoplanet Exploration Program and built at the NASA Ames Research Center by Steve B. Howell, Nic Scott, Elliott P. Horch, and Emmett Quigley. 'Alopeke was mounted on the Gemini North telescope of the international Gemini Observatory, a program of NSF's OIR Lab, which is managed by the Association of Universities for Research in Astronomy (AURA) under a cooperative agreement with the National Science Foundation. On behalf of the Gemini partnership: the National Science Foundation (United States), National Research Council (Canada), Agencia Nacional de Investigación y Desarrollo (Chile), Ministerio de Ciencia, Tecnología e Innovación (Argentina), Ministério da Ciência, Tecnologia, Inovações e Comunicações (Brazil), and Korea Astronomy and Space Science Institute (Republic of Korea). This work makes use of observations from the LCOGT network. Part of the LCOGT telescope time was granted by NOIRLab through the Mid-Scale Innovations Program (MSIP). MSIP is funded by NSF. This paper makes use of observations made with the MuSCAT2 instrument, developed by the Astrobiology Center, at TCS operated on the island of Tenerife by the IAC in the Spanish Observatorio del Teide. This paper is based on observations made with the MuSCAT3 instrument, developed by the Astrobiology Center and under financial supports by JSPS KAKENHI (JP18H05439) and JST PRESTO (JPMJPR1775), at Faulkes Telescope North on Maui, HI, operated by the Las Cumbres Observatory. This research has made use of the Exoplanet Follow-up Observation Program (ExoFOP; DOI:10.26134/ExoFOP5) website, which is operated by the California Institute of Technology, under contract with the National Aeronautics and Space Administration under the Exoplanet Exploration Program. This publication makes use of data products collected by the TESS mission and obtained from the MAST data archive at the Space Telescope Science Institute (STScI). The light curve and target pixel file data used in this paper can be found in 10.17909/t9-nmc8-f686. C.M. would like to gratefully acknowledge the entire Dragonfly Telephoto Array team, and Bob Abraham in particular, for allowing their telescope bright time to be put to use observing exoplanets. TRAPPIST-South is funded by the Belgian National Fund for Scientific Research (F.R.S.-FNRS) under grant PDR T.0120.21, with the participation of the Swiss National Science Fundation (SNF). M.G. is F.R.S-FNRS Research Director. E.J. is F.R.S-FNRS Senior Research Associate. The postdoctoral fellowship of KB is funded by F.R.S.-FNRS grant T.0109.20 and by the Francqui Foundation. This publication benefits from the support of the French Community of Belgium in the context of the FRIA Doctoral Grant awarded to MT. F.J.P. acknowledges financial support from the grant CEX2021-001131-S funded by MCIN/AEI/ 10.13039/501100011033. This research received funding from the European Research Council (ERC) under the European Union's Horizon 2020 research and innovation program (grant agreement n° 803193/BEBOP), and from the Science and Technology Facilities Council (STFC; grant n° ST/S00193X/1). This work makes use of observations from the ASTEP telescope. ASTEP benefited from the support of the French and Italian polar agencies IPEV and PNRA in the framework of the Concordia station program, from INSU, ESA, the University of Birmingham, and STFC.

Software: `TLS` (Hippke & Heller 2019), `LATTE` (Eisner 2022), `TESS-Plots`,[48] `Lightkurve` (Lightkurve Collaboration et al. 2018), `Juliet` (Espinoza et al. 2018), and `TRICERATOPS` (Giacalone & Aressing 2020).

Appendix
Nearby Stars and their Probability being a Nearby Planet or Nearby Eclipsing Binary

In Table 7, we have compiled a list of nearby stars for which nonzero transit depths were measured using the `TRICERATOPS` tool. These stars were selected as targets to calculate the

[48] https://github.com/mkunimoto/TESS-plots

Table 7
All the Nearby Stars Considered by TRICERATOPS to Calculate NFPP

Target	Nearby TICs	Separation (arcsec)	Transit Depth	Probability		
				NTP[i]	NEB[ii]	NEBX2P[iii]
TOI-139	…	…	…	…	…	-
TOI-672	151825526	51.797	0.5419	0.00E+00	1.45E-46	5.58E-72
TOI-913	407126405	9.538	0.0672	2.49E-69	1.80E-63	1.29E-57
	407126402	46.165	0.1389	1.13E-69	3.67E-68	9.97E-67
	407126397	58.015	0.3984	9.14E-70	5.68E-28	1.15E-26
	407126407	63.915	0.7803	1.75E-70	2.48E-70	1.71E-70
	407126425	99.975	0.5770	1.29E-70	1.06E-70	2.28E-71
TOI-1694	396776943	52.393	0.8128	0.00E+00	9.63E-100	1.42E-132
	396740632	79.123	0.7012	0.00E+00	8.27E-158	3.04E-157
TOI-2194	…	…	…	…	…	-
TOI-2443	318753384	54.738	0.5893	0.00E+00	5.58E-64	9.21E-89
	318753383	62.408	0.1128	2.20E-200	1.54E-19	3.04E-35
TOI-2459	192790481	18.900	0.1217	1.19E-21	8.85E-05	1.59E-09
	192790483	51.229	0.0585	1.04E-54	1.80E-04	1.43E-09
	192790473	72.392	0.1829	8.46E-41	2.26E-06	5.33E-10
TOI-3082	428699131	21.134	0.0572	2.75E-59	4.76E-28	8.90E-29
TOI-4308	144193716	44.501	0.6594	3.36E-16	5.48E-11	1.19E-10
TOI-5704	900281091	2.587	0.1832	1.79E-17	5.24E-04	2.94E-05
TOI-5803	466382573	64.612	0.6685	1.77E-58	5.15E-08	6.46E-11

Notes.
[i] Nearby transiting planet.
[ii] Nearby eclipsing binary.
[iii] Nearby eclipsing binary with an orbital period twice of what we are getting from the analysis of a signal.

NFPP. The NFPP values were then presented in Table 4. Specifically, an NFPP value of 0.00 ± 0.00 suggests that there is no known nearby star for which a nonzero transit depth has been observed.

ORCID iDs

Priyashkumar Mistry https://orcid.org/0000-0002-4903-7950
Kamlesh Pathak https://orcid.org/0000-0001-9365-6137
Aniket Prasad https://orcid.org/0000-0002-8823-8835
Georgios Lekkas https://orcid.org/0000-0003-3559-0840
Surendra Bhattarai https://orcid.org/0000-0001-9026-8622
Sarvesh Gharat https://orcid.org/0000-0003-4845-7141
Mousam Maity https://orcid.org/0000-0002-1918-4749
Dhruv Kumar https://orcid.org/0000-0001-8205-0404
Karen A. Collins https://orcid.org/0000-0001-6588-9574
Richard P. Schwarz https://orcid.org/0000-0001-8227-1020
Christopher R. Mann https://orcid.org/0000-0002-9312-0073
Elise Furlan https://orcid.org/0000-0001-9800-6248
Steve B. Howell https://orcid.org/0000-0002-2532-2853
David Ciardi https://orcid.org/0000-0002-5741-3047
Allyson Bieryla https://orcid.org/0000-0001-6637-5401
Elisabeth C. Matthews https://orcid.org/0000-0003-0593-1560
Erica Gonzales https://orcid.org/0000-0002-9329-2190
Carl Ziegler https://orcid.org/0000-0002-0619-7639
Ian Crossfield https://orcid.org/0000-0002-1835-1891
Steven Giacalone https://orcid.org/0000-0002-8965-3969
Thiam-Guan Tan https://orcid.org/0000-0001-5603-6895
Phil Evans https://orcid.org/0000-0002-5674-2404
Krzysztof G. Hełminiak https://orcid.org/0000-0002-7650-3603
Kevin I. Collins https://orcid.org/0000-0003-2781-3207
Norio Narita https://orcid.org/0000-0001-8511-2981
Akihiko Fukui https://orcid.org/0000-0002-4909-5763
Francisco J. Pozuelos https://orcid.org/0000-0003-1572-7707
Courtney Dressing https://orcid.org/0000-0001-8189-0233
Abderahmane Soubkiou https://orcid.org/0000-0002-0345-2147
Zouhair Benkhaldoun https://orcid.org/0000-0001-6285-9847
Joshua E. Schlieder https://orcid.org/0000-0001-5347-7062
Olga Suarez https://orcid.org/0000-0002-3503-3617
Khalid Barkaoui https://orcid.org/0000-0003-1464-9276
Enric Palle https://orcid.org/0000-0003-0987-1593
Felipe Murgas https://orcid.org/0000-0001-9087-1245
Maria V. Goliguzova https://orcid.org/0000-0003-2228-7914
Ivan A. Strakhov https://orcid.org/0000-0003-0647-6133
Crystal Gnilka https://orcid.org/0000-0003-2519-6161
Kathryn Lester https://orcid.org/0000-0002-9903-9911
Colin Littlefield https://orcid.org/0000-0001-7746-5795
Nic Scott https://orcid.org/0000-0003-1038-9702
Rachel Matson https://orcid.org/0000-0001-7233-7508
Michaël Gillon https://orcid.org/0000-0003-1462-7739

Emmanuel Jehin https://orcid.org/0000-0001-8923-488X
Mourad Ghachoui https://orcid.org/0000-0003-3986-0297
Lyu Abe https://orcid.org/0000-0002-0856-4527
Philippe Bendjoya https://orcid.org/0000-0002-4278-1437
Tristan Guillot https://orcid.org/0000-0002-7188-8428
Amaury H. M. J. Triaud https://orcid.org/0000-0002-5510-8751

References

Brown, T. M. 2003, ApJL, 593, L125
Brown, T. M., Baliber, N., Bianco, F. B., et al. 2013, PASP, 125, 1031
Bryson, S. T., Jenkins, J. M., Gilliland, R. L., et al. 2013, PASP, 125, 889
Buchhave, L. A., Bizzarro, M., Latham, D. W., et al. 2014, Natur, 509, 593
Buchhave, L. A., Latham, D., Johansen, A., et al. 2012, Natur, 486, 375
Cameron, A. C. 2012, Natur, 492, 48
Chen, J., & Kipping, D. 2017, ApJ, 834, 17
Collins, K. A., Kielkopf, J. F., Stassun, K. G., & Hessman, F. V. 2017, AJ, 153, 77
Collins, K. 2019, AAS Meeting Abstracts, 233, 140.05
Díaz, R. F., Almenara, J. M., Santerne, A., et al. 2014, MNRAS, 441, 983
Eastman, J. D., Rodriguez, J. E., Agol, E., et al. 2019, arXiv:1907.09480
Eisner, N. L. 2022, LATTE: Lightcurve Analysis Tool for Transiting Exoplanet, Astrophysics Source Code Library, ascl:2205.006
Espinoza, N., Kossakowski, D., & Brahm, R. 2018, Juliet: Transiting and non-transiting exoplanetary systems modelling tool, Astrophysics Source Code Library, ascl:1812.016
Fűrész, G. 2008, PhD thesis, University of Szeged, Hungary
Fortier, A. 2014, 40th COSPAR Scientific Assembly, 40, E1.14
Furlan, E., Ciardi, D. R., Everett, M. E., et al. 2017, AJ, 153, 71
Gardner, J. P., Mather, J. C., Clampin, M., et al. 2006, SSRv, 123, 485
Gavel, D., Kupke, R., Dillon, D., et al. 2014, Proc. SPIE, 9148, 914805
Giacalone, S., & Dressing, C. D. 2020, triceratops: Candidate exoplanet rating tool, Astrophysics Source Code Library, ascl:2002.004
Giacalone, S., Dressing, C. D., Jensen, E. L. N., et al. 2021, AJ, 161, 24
Guillot, T., Abe, L., Agabi, A., et al. 2015, AN, 336, 638
Habets, G. M. H. J., & Heintze, J. R. W. 1981, A&AS, 46, 193
Hayward, T. L., Brandl, B., Pirger, B., et al. 2001, PASP, 113, 105
Hippke, M., & Heller, R. 2019, A&A, 623, A39
Horch, E. P., Veillette, D. R., Baena Gallé, R., et al. 2009, AJ, 137, 5057
Howell, S. B., Everett, M. E., Sherry, W., Horch, E., & Ciardi, D. R. 2011, AJ, 142, 19
Jensen, E. 2013, Tapir: A web interface for transit/eclipse observability, Astrophysics Source Code Library, ascl:1306.007
Kempton, E. M. R., Bean, J. L., Louie, D. R., et al. 2018, PASP, 130, 114401
Kostov, V. B., Mullally, S. E., Quintana, E. V., et al. 2019, AJ, 157, 124
Kunimoto, M., Winn, J., Ricker, G. R., & Vanderspek, R. K. 2022, AJ, 163, 290
Kupke, R., Gavel, D., Roskosi, C., et al. 2012, Proc. SPIE, 8447, 84473G
Lenzen, R., Hofmann, R., Bizenberger, P., & Tusche, A. 1998, Proc. SPIE, 3354, 606
Lindegren, L. 2018, http://www.rssd.esa.int/doc_fetch.php?id=3757412
Lightkurve Collaboration, Cardoso, J. V. D. M., Hedges, C., et al. 2018, Lightkurve: Kepler and TESS time series analysis in Python, Astrophysics Source Code Library, ascl:1812.013
McCully, C., Volgenau, N. H., Harbeck, D.-R., et al. 2018, Proc. SPIE, 10707, 107070K
McGurk, R., Rockosi, C., Gavel, D., et al. 2014, Proc. SPIE, 9148, 91483A
Mékarnia, D., Guillot, T., Rivet, J. P., et al. 2016, MNRAS, 463, 45
Mistry, P., Pathak, K., Lekkas, G., et al. 2023, MNRAS, 521, 1066
Morton, T. D. 2015, VESPA: False positive probabilities calculator, Astrophysics Source Code Library, ascl:1503.011
Narita, N., Fukui, A., Kusakabe, N., et al. 2019, JATIS, 5, 015001
Narita, N., Fukui, A., Yamamuro, T., et al. 2020, Proc. SPIE, 11447, 114475K
Parviainen, H., Tingley, B., Deeg, H. J., et al. 2019, A&A, 630, A89
Rauer, H., Aerts, C., Deleuil, M., et al. 2022, EPSC Abstracts, 16, EPSC2022–453
Ricker, G. R., Winn, J. N., Vanderspek, R., et al. 2015, JATIS, 1, 014003
Rousset, G., Lacombe, F., Puget, P., et al. 2000, Proc. SPIE, 4007, 72
Safonov, B. S., Lysenko, P. A., & Dodin, A. V. 2017, AstL, 43, 344
Sakai, S., Lu, J. R., Ghez, A., et al. 2020, ApJ, 873, 65
Savel, A. B., Dressing, C. D., Hirsch, L. A., et al. 2020, AJ, 160, 287
Savel, A. B., Hirsch, L. A., Gill, H., Dressing, C. D., & Ciardi, D. R. 2022, PASP, 134, 124501
Schlieder, J. E., Gonzales, E. J., Ciardi, D. R., et al. 2021, FrASS, 8, 63
Schmider, F.-X., Abe, L., Agabi, A., et al. 2020, Proc. SPIE, 12182, 121822O
Scott, N. J., Howell, S. B., Gnilka, C. L., et al. 2021, FrASS, 8, 138
Stassun, K. G., Oelkers, R. J., Paegert, M., et al. 2019, AJ, 158, 138
Stassun, K. G., Oelkers, R. J., Pepper, J., et al. 2018, AJ, 156, 102
Telting, J. H., Avila, G., Buchhave, L., et al. 2014, AN, 335, 41
Tokovinin, A., Mason, B. D., & Hartkopf, W. I. 2010, AJ, 139, 743
Torres, G., Konacki, M., Sasselov, D. D., & Jha, S. 2005, ApJ, 619, 558
Van Zandt, J., Petigura, E. A., MacDougall, M., et al. 2023, AJ, 165, 60
Weidner, C., & Vink, J. S. 2010, A&A, 524, A98
Wizinowich, P., Acton, D. S., Shelton, C., et al. 2000, PASP, 112, 315
Ziegler, C., Tokovinin, A., Briceño, C., et al. 2020, AJ, 159, 19
Ziegler, C., Tokovinin, A., Latiolais, M., et al. 2021, AJ, 162, 192